INFORMATION TO USERS

This manuscript has been reproduced from the microfilm master. UMI films the text directly from the original or copy submitted. Thus, some thesis and dissertation copies are in typewriter face, while others may be from any type of computer printer.

The quality of this reproduction is dependent upon the quality of the copy submitted. Broken or indistinct print, colored or poor quality illustrations and photographs, print bleedthrough, substandard margins, and improper alignment can adversely affect reproduction.

In the unlikely event that the author did not send UMI a complete manuscript and there are missing pages, these will be noted. Also, if unauthorized copyright material had to be removed, a note will indicate the deletion.

Oversize materials (e.g., maps, drawings, charts) are reproduced by sectioning the original, beginning at the upper left-hand corner and continuing from left to right in equal sections with small overlaps.

ProQuest Information and Learning
300 North Zeeb Road, Ann Arbor, MI 48106-1346 USA
800-521-0600

SOLID STATE NMR STUDY OF SEI FORMATION IN LITHIUM ION BATTERIES

by

Dachun Zhao

A dissertation submitted to the Graduate Faculty in Physics in partial fulfillment of the requirements for the degree of Doctor of Philosophy, The City University of New York

2004

UMI Number: 3115305

ProQuest Information and Learning Company
300 North Zeeb Road
P.O. Box 1346
Ann Arbor, MI 48106-1346

This manuscript has been read and accepted for the Graduate Faculty in Physics in satisfaction of the dissertation requirement for the degree of Doctor of Philosophy.

11/24/03
Date

Professor Marten denBoer, Chair of Examining Committee

11/24/03
Date

Professor Sultan Catto, Executive Officer

Professor Ying-Chih Chen

Professor Mark Hillery

Professor Louis Massa

Professor Steven A.Schwarz

Supervisory Committee

THE CITY UNIVERSITY OF NEW YORK

ABSTRACT

SOLID STATE NMR STUDY OF SEI FORMATION IN LITHIUM ION BATTERIES

by

Dachun Zhao

Advisor: Marten denBoer

Recently, rechargeable lithium ion batteries, which offer high energy density and long cycle life, are in great demand as power sources for our mobile electronic society. The formation of a solid electrolyte interphase (SEI) on the surface of electrodes in lithium ion batteries plays an essential role in their performance. This thesis presents solid state NMR and MAS NMR results on the SEI, which contribute to our understanding of SEI formation on both cathodes and anodes.

This thesis is organized as following: Chapter 1 surveys the history of batteries and the challenges to further development of the lithium ion battery. Fundamental aspects and SEI formation mechanisms are also included in Chapter 1. Chapter 2 deals with the principles and experimental techniques of solid state NMR.

Chapter 3 presents studies of SEI formation on anode and cathode in lithium ion batteries using electrochemical impedance spectroscopy (EIS) and NMR. The results provide EIS and NMR evidence that cells containing electrolytes with high EC content display less irreversible capacity after high temperature storage. The irreversible capacity is attributed to SEI growth on electrode surfaces. NMR results on cathodes, on the other hand, imply that the presence of Ni in the cathode may reduce cell

performance due to the oxidation of Ni^{3+} to Ni^{4+}. Our simulations show that a lower EC/DMC ratio is associated with a smaller SEI intensity for the cathode and higher intensity for the anode.

Chapter 4 discusses the effect of temperature on SEI formation on anodes and cathodes. NMR measurements show that MCMB graphite based anodes exhibit high stability no chemical shift is evident over a wide temperature range. On cathodes, however, NMR does reveal changes in SEI intensity as a function of temperature. These changes are believed to be the result of decomposition of the SEI. Evidently, then, changes in the performance of the cell as a factor of temperature are, at least in part, due to changes in the SEI with temperature.

In Chapter 5 we report on the use of NMR to study the effect of electrolyte/solvent and electrode structure on SEI formation. The intensity of the SEI in a cell containing LiBOB electrolyte with EC and DEC is greater than that in a cell with $LiPF_6$ electrolyte with EC and DMC. This implies that the cell containing LiBOB electrolyte with EC and DEC is more stable. From the analysis of NMR of the cathode, it was found that it is easier to form SEI in layered structure cathode than in a spinel structure, suggesting that spinel structure materials may be better choices as cathode in lithium ion batteries. Evidently, then, the choice of electrolyte/solvent materials and electrode materials are key factors in determining the performance of lithium ion batteries.

ACKNOWLEDGMENTS

I would like to thank Professor Marten denBoer and Steve Greenbaum, for guidance, suggestion and comments on my final thesis.

I would like to thank the committee:Professor Ying-Chih Chen, Professor Mark Hillery, Professor Louis Massa, and Professor Steven A.Schwarz for taking time.

I would like to thank Professor Sultan Catto, Professor Godfrey Gumbs and Professor Ying-Chih Chen help me go through all the difficulties at Hunter.

Special thanks should go to Dr. Jun Liu and Dr. Smart for helping the preparation of the samples.

Finally, I dedicate my gratefulness to my wife Dr. L. Xu, my daughter Amy, my parents and parents-in-law who always show me understanding and support.

Table of Contents

List of Figures

List of Tables

Chapter 1 General introduction

1.1 Overview of lithium ion battery

1.1.1 Brief history

The batteries that power portable electronic devices are based on concepts dating from two centuries ago. The first battery is invented by Alessandro Volta in 1799[1]. Materials used in the original voltaic pile were zinc and silver plates and a porous non-conducting separator saturated with sea water. The first rechargeable battery was demonstrated by Johann Ritler in 1802. However, this rechargeable battery remained a laboratory study for many years until Gason Plate developed the chemical reaction of the lead-acid battery in 1860 and Foure developed pasted lead electrodes in 1881. The most successful rechargeable Ni-Cd battery operating on an electrochemical process was developed by Waldemar Jungner in 1901. The alkaline nickel-iron battery, consisting of a metallic iron negative electrode and a nickel hydroxide compound electrode immersed in concentrated potassium hydroxide electrolyte, was developed in 1910.

Fundamental early studies on lithium batteries began in the 1950's when it was found that lithium metal is stable in some nonaqueous electrolytes and $LiClO_4$ electrolyte in a propylene carbonate. Primary lithium batteries, such as the Li-MnO_2 cell, were produced in the early 1970's. Since 1972[1, 2], the lithium-iodine battery has been used successfully to power more than 4 million cardiac pacemakers. Rechargeable lithium batteries using Li metal as an anode, and transition metal TM chalcogenides (TiS_2, etc) or TM oxides (V_2O_5, MnO_2, etc) as cathode were developed in the mid 1970's. However, the advanced lithium ion battery concept or "rocking chair" cell was

proposed in 1980's [3, 4]. The situation changed radically in 1991 when Sony Energetic Inc. announced commercial lithium ion batteries. Important parameters of some commercial lithium ion battery are summarized in Table 1.

Table 1.Energy density of some commercial lithium ion batteries

Cell	Energy density	
	Gravimetric(Wh/kg)	Volumetric(Wh/l)
Sony US18650	103	245
A&T LSR 18650	130	321
Sanyo UR 18650	126	288
Moli ICR 18650	113	287
Matsushita CGR 17500	129	269
SAFT VL 18650	108	260

1.1.2 Classification of battery

Batteries are classified either as primary or secondary batteries according to whether they are rechargeable or not. Rechargeable batteries are often categorized based on the material of electrodes. Today's most common rechargeable batteries are [5, 6, 7, 8, 9]:

- Sealed lead acid (SLA): most economical for larger power applications where weight is lesser concern, for example, motor vehicles, medical equipment, wheelchairs, UPS systems, and emergency lighting.
- Nickel cadmium (Ni-Cd): main applications are portable radios, emergency medical equipment, video cameras and power tool.
- Nickel metal hydride (Ni-MH): applications include cellular phones and laptop computers.
- Lithium and lithium ion battery: applications include notebook computers, video cameras, new generation cellular phones, and advanced military communication devices, etc.

In addition, among other modern battery system are: rechargeable alkaline manganese, zinic-nickel, and silver-zinc. The characteristics and electrode chemical reactions of the most commonly used rechargeable battery are summarized in Table 2 [5, 6, 7, 8, 9].

1.2 The principle of lithium and lithium ion battery

Many efforts to develop rechargeable lithium battery followed in 1980's[10,11], but failed due to safety concerns. Generally, there are two kinds of lithium related battery, one based on a metallic lithium anode, called lithium battery, the other based on an intercalation compound anode, for example, graphite, called lithium ion battery. For both kinds of batteries, lithium transition metal oxide serves as cathode. The main

Table 2. Electrodes reaction in several major types of rechargeable battery

Cell type	(+)Cathode (-)Anode	Electrode reaction	E^0(V)
Lead-acid	+	$PbSO_4+2H_2O \leftrightarrow PbO_2 +3H^+ +HSO_4^- +2e^-$	1.68V
	-	$PbSO_4+2e^- \leftrightarrow Pb + HSO_4^-$	0.36V
	overall	$2\ PbSO_4 +2H_2O \leftrightarrow Pb+ PbO_2+2H_2SO_4$	2.04V
Nickel-cadmium (Ni-Cd)	+	$2Ni(OH)_2+2OH^- \leftrightarrow 2HNiO_2+2H_2O+2e^-$	0.52V
	-	$Cd(OH)_2+2e^- \leftrightarrow Cd+2\ OH^-$	0.81V
	overall	$2Ni(OH)_2+ Cd(OH)_2 \leftrightarrow Cd+2HNiO_2+2H_2O$	1.33V
Nickel-metal hydride (NiMH)	+	$2Ni(OH)_2+2OH^- \leftrightarrow 2HNiO_2+2H_2O+2e^-$	0.52V
	-	$M+H_2O+e^- \leftrightarrow MH+2\ OH^-$	0.83V
	Overall	$Ni(OH)_2+M \leftrightarrow HNiO_2+MH$	1.35V
Lithium ion cell	+	$Li_{(1-x)}CoO_2 \leftrightarrow CoO_2$	x
	-	$Li_{(1-x)}CoO_2 +C \leftrightarrow CoO_2+Li_xC$	x
	overall	$LiCoO_2 +C \leftrightarrow CoO_2+Li_xC$	3.6V

advantage of lithium ion batteries compared with other rechargeable batteries are their high energy density, long cycle-life and no "memory effect". The principle of the two main types of lithium rechargeable battery and electrode chemical reaction are illustrated in Fig.1 (a, b).

1.3 General considerations of lithium ion battery

1.3.1 Electrochemical process

The basic principles of reversible energy storage in cathode and anode material for lithium ion battery are dependent on a reversible insertion reaction, a so - called

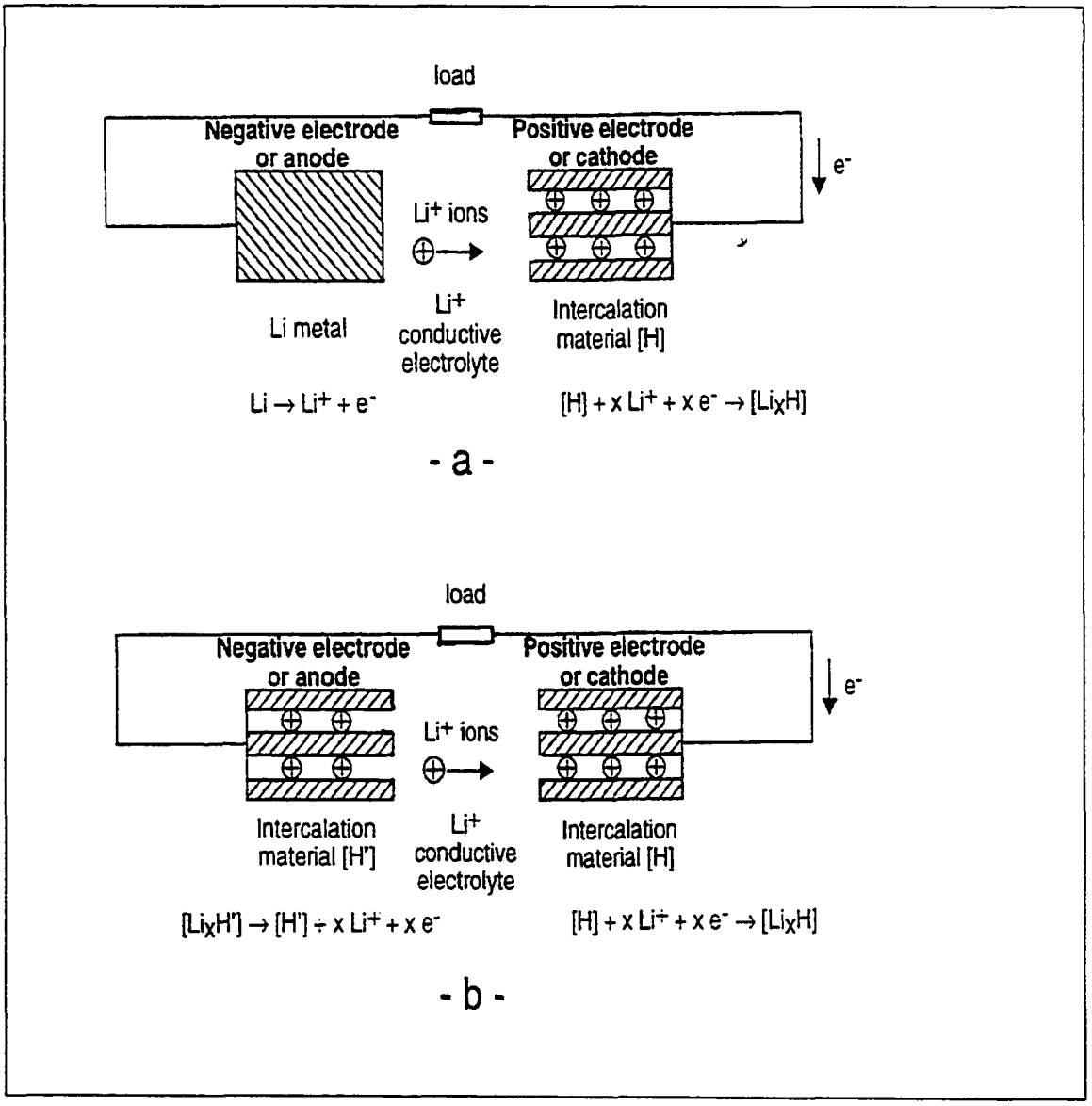

Fig.1 (a, b) Schematic of lithium and lithium ion battery, a: lithium battery, b: lithium ion battery.

intercalation reaction. An intercalation reaction involves the topotactic occupation by a guest species of initially empty sites of the host framework [H], without breaking of strong bonds within the solid structure, leading to a solid showing close structural relationship with the starting compound, so that the reaction is truly reversible [12, 13, 14]. In the case of a lithium ion battery, such a reversible reaction may be written as:

$$[H] + x\ Li^+ + x\ e^- \Leftrightarrow [Li_xH]$$

where H is the host species. The change in free energy of reaction (ΔG^o) is related to the battery potential (E) by the following equation [15]:

$$E = -\frac{\Delta G^0}{nF} = \frac{\mu_a - \mu_c}{F}$$

where n is the number of electrons, F the Faraday constant (96500C/mol), and μ the chemical potential of electrodes. On the other hand, thermodynamic stability of the electrolyte requires that its lowest unoccupied state have a higher energy than the highest occupied state of reductant, that its highest occupied state have a lower energy than the lowest unoccupied state of the oxidant. Fig. 2 shows a schematic energy level diagram for a lithium or lithium ion battery [16].

1.3.2 General requirement and fundamental concepts

The main requirements for the electrode in the lithium ion battery that are determined by material characteristics such as structure, composition and morphology are as follows:

- High energy density: Energy density is the amount of energy stored within a cell per unit weight (the gravimetric density, in $Whkg^{-1}$) or per unit volume (the volumetric density, in WhL^{-1}).

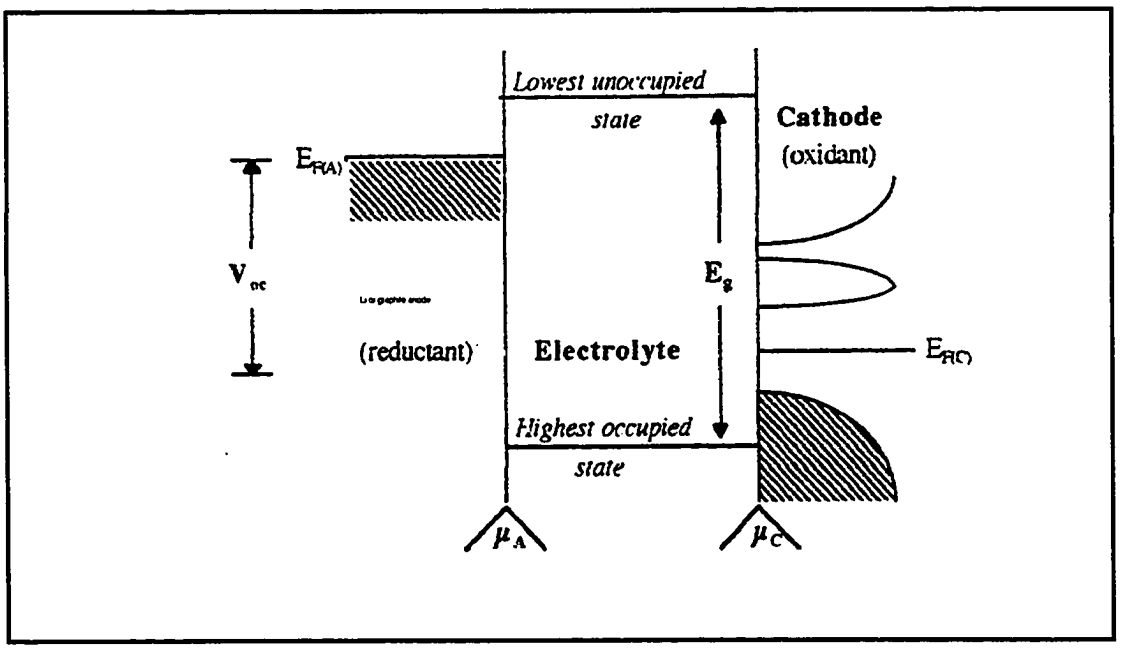

Fig. 2 Schematic energy level diagram for a lithium or lithium ion battery [16].

- Long cycle life: number of charge –discharge cycles that a cell survives before its capacity falls below an acceptable level.
- Thermal and chemical stability, good performance in a wide temperature range.
- Non-toxicity, friendly to environment.
- Low cost.

1.4Advanced material for lithium ion battery

Many materials have been studied for use in lithium ion batteries. Especially, lithium transition metal oxides (LiM_xO_2, M: transition metal) such as $LiNiO_2$ and $LiCoO_2$ or lithium transition metal mixed oxide compounds ($LiM_1M_2O_2$, M_1 and M_2 are transition metal), such as $LiNi_{0.8}Co_{0.2}O_2$, have been used as active cathode material as a positive electrode, and various types of graphite based anodes are commonly used in commercial lithium ion battery industry. This is because lithium transition metal oxide cathodes exhibit a larger discharge capacity and structural stable properties than other lithium compounds. A graphite based anode has good cycle performance compared with lithium metal or lithium alloy used as a negative electrode in lithium ion batteries. The following section deals with lithium transition metal oxide, graphite based materials, electrolyte and electrolyte solvent that are used in lithium ion batteries.

1.4.1 Cathode material

As noted above, a variety of lithium transition metal oxide $LiMO_2$ (M= Co, Ni, Mn, V, etc), both layered and spinel structure, has been studied for cathode in lithium ion battery system. Many methods [17, 18, 19, 20], such as solid state reaction (high temperature), solution reaction (wet method, low temperature) including hydrothermal, ion exchange, sol-gel, aerogel, xerogel, etc, have been used to prepare cathode material. At present, although the most popular cathode in commercial lithium ion batteries is $LiCoO_2$, $LiNiO_2$ and $LiMn_2O_4$ have advantage in energy density and cost. In particular, $LiMn_2O_4$ has been the most attractive potential cathode due to its

non-toxicity and low cost. Table 3 shows some performance characteristics of lithium transition metal oxide cathodes.

Table 3 The characteristics of lithium transition metal oxide cathodes.

Cathode	Capacity(Ah/g)	Average voltage	cost	toxicity
$LiCoO_2$	0.18	3.9	very high	high
$LiNiO_2$	0.22	3.8	fair	fair
$LiMn_2O_4$	0.12	4.0	low	low

The ideal layered $LiMO_2$ (M=Ni, Co) cathode has a rhombohedral structure where Li^+ and M cations occupy in the octahedral interstitial sites in closed packed oxygen array of space group $R\bar{3}m$, in such a way that MO_2 layers are formed consisting of edge-sharing $[MO_6]$ octahedral. Such a layered structure provides a 2-D diffusion path for Li^+ . In between these layers Li^+ resides in octahedral $[LiO_6]$ coordination, leading to alternating (111) planes of cubic rock salt structure. For ideal spinel $LiMn_2O_4$ structure, oxygen atoms form a face-centered cubic packing and occupy 32e sites of space group Fd3m. The Li^+ ions are located at the tetrahedral 8a sites, while Mn^{3+} occupies the octahedral 16d sites; the octahedral 16c sites remain empty. Li^+ ions are mobile within 3-D channels with a 8a-16c-8a diffusion path. Typical layered and spinel structure of $LiMO_2$ [21, 22, 8] are illustrated in Fig.3.

1.4.2 Anode material

Graphite based anode materials are commonly used in lithium ion batteries due to their relatively high specific capacity, good cyclability, thermal stability with most

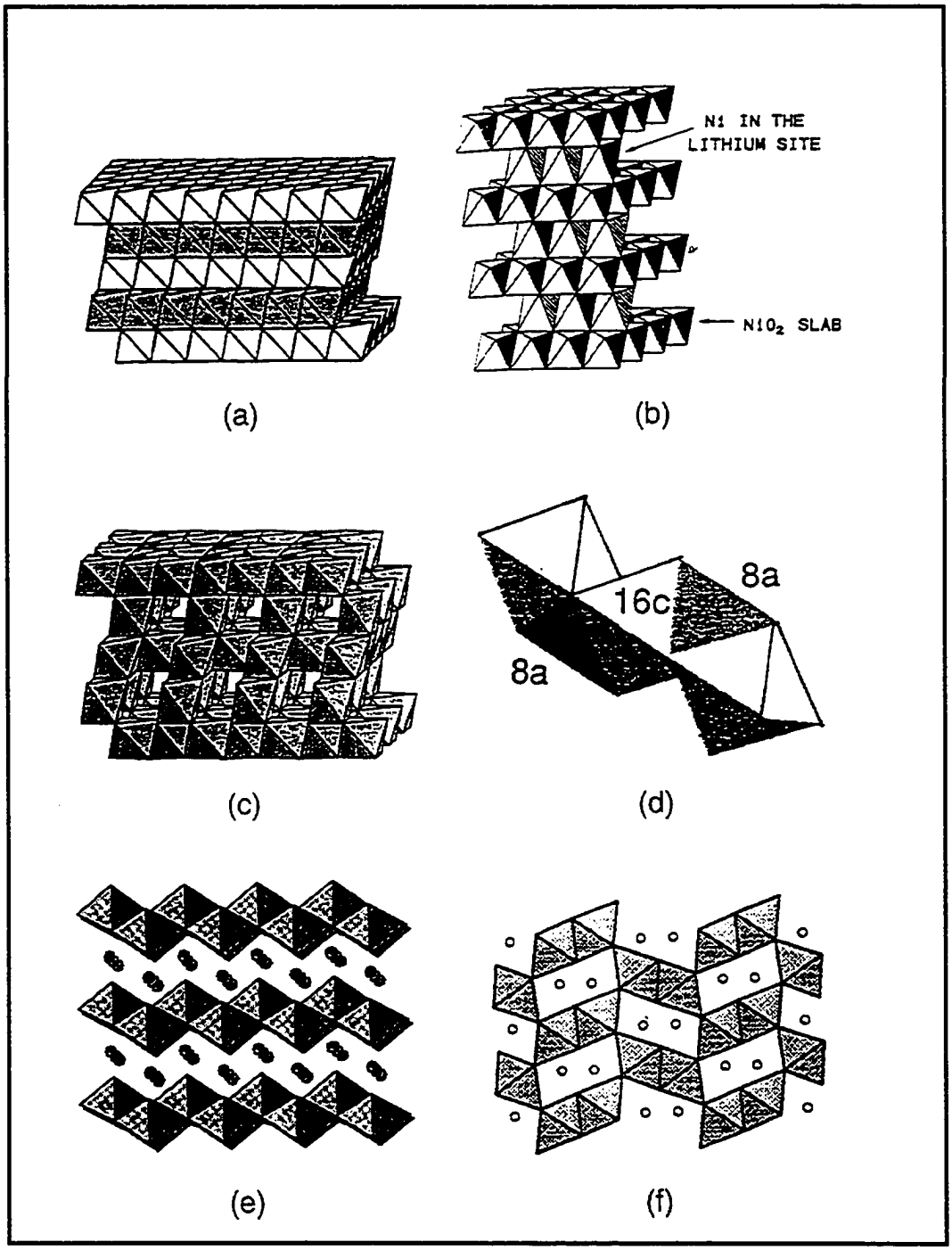

Fig.3 Typical layered and spinel structure of cathode material. a: layered, b: quasi-layered, c: spinel, d: diffusion path (8a-16c-8a), e: corrugated layered, f: ramsdellite-partial structure

electrolytes and safety compared with lithium metal anode, nontoxic and low cost. The types of carbonaceous materials used in lithium ion batteries are roughly divided into three groups:

- Graphite.
- Soft carbon made from coal or petroleum pitches, which form graphite on treatment at high temperature (> 2400 °C).
- Hard carbon, which does not form graphite even at T > 3000 °C.

Typical structures of three types of carbon are shown in Fig. 4 [23].

Graphite is one of the three allotropic forms of carbon, besides diamond and the fullerenes family (with C_{60} as main element). As shown in Fig. 4, graphite is a 2-D network composed of stacked carbon layers. Carbon is in the sp^2 orbital hybridization sharing σ type covalent bonding within the layers. The in plane carbon-carbon distance is 0.142 nm and the spacing between layers is 0.335 nm. Under certain conditions, graphite can store Li ions electrochemically, forming graphite intercalation compounds (GIC). The storage process is reversible and can be expressed as the following equation:

$$nC + I \Leftrightarrow C_n I$$

where I is an intercalate "I" guest, Li^+, for example, and an n is an integer. The mechanism of intercalation dynamics is illustrated in Fig. 5.

As illustrated in Fig. 5, this intercalation reaction generally follows a stepwise mechanism, that is, not all the inter-layer available space will be occupied by the guest species. Actually, the latter will be distributed along the c-axis with some periodicity.

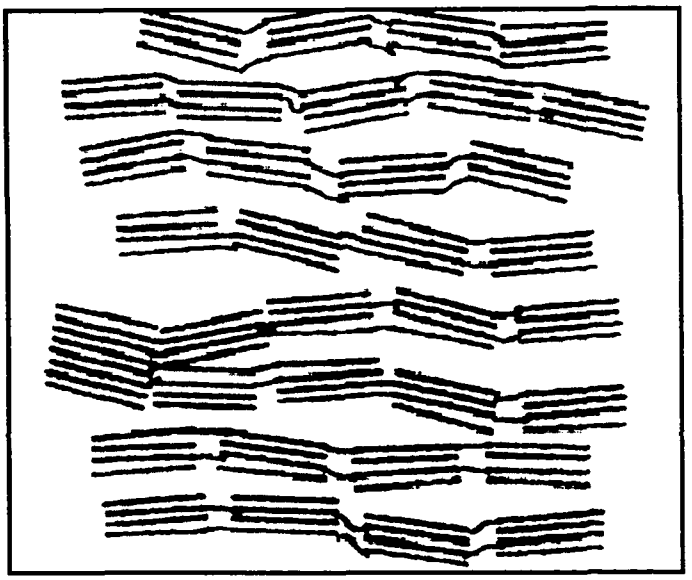

Soft carbon

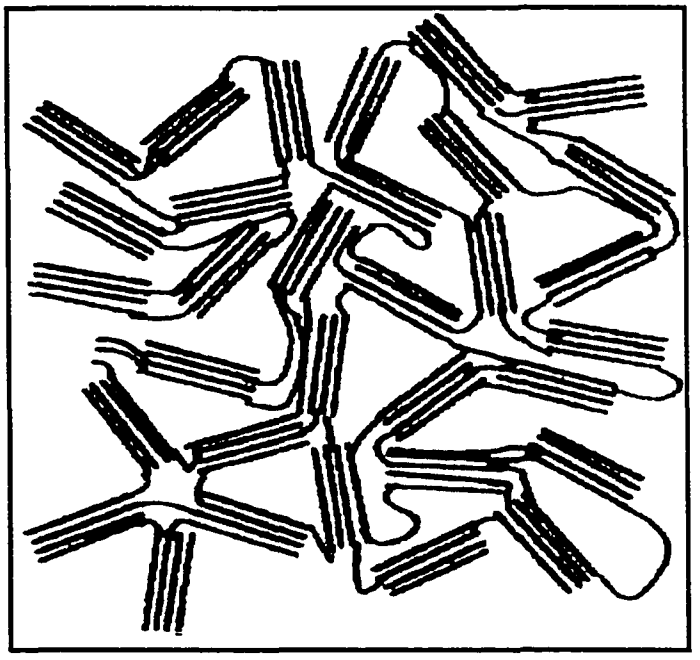

Hard carbon

Fig. 4 Structure of three types of carbon [23]

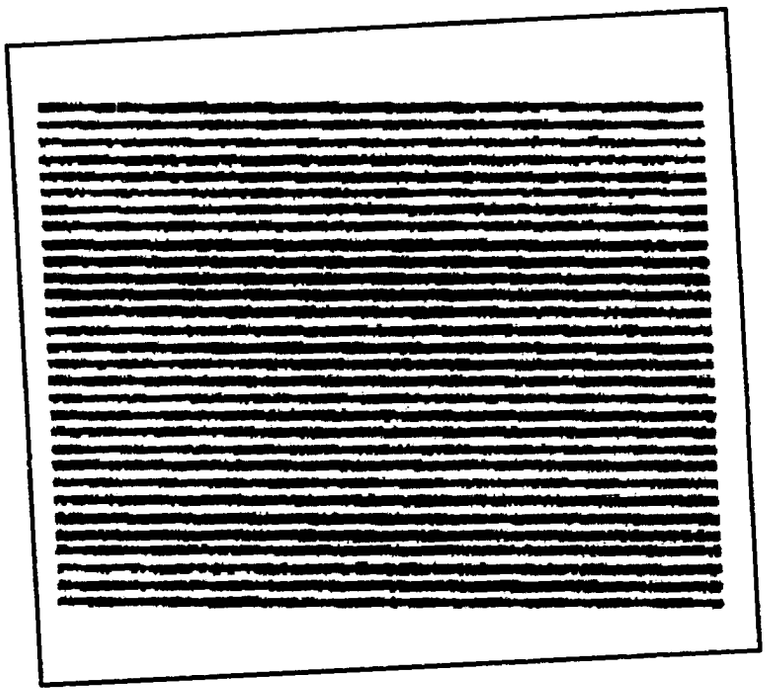

Graphite

Fig. 4 Cont'd

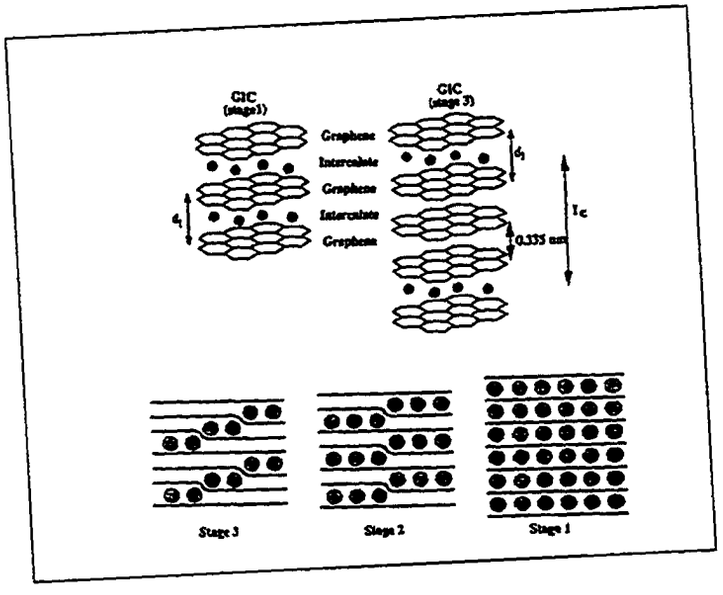

Fig. 5 Intercalation dynamics and stage formation in GIC.[3]

The number of graphenes between two intercalate layers is called the intercalation stage. Therefore, in stage-3 GIC, three graphenes separate two adjacent intercalate layers and in stage 2 and 1, only two and one graphene respectively separate them.

Deintercalation may follow the reciprocal mechanism, going from lower stage to higher ones. The relationship between stoichiometry and stage is not that obvious, although the composition of lower stages can be predicted taking into account geometric effect and the charge transfer which controls in-plane and out-of –plane interaction.

1.4.3 Electrolyte and solvents

The lithium ion battery as a power source is designed to be used up to about 4.0 V. At high operating voltage, only organic solvents which can withstand oxidation and decomposition can be used with the combination of Li salts as electrolytes. There are two groups of electrolytes in use or under development. One is a liquid solution of Li salts in aprotic organic solvents, the other, is polymer electrolyte such as polyethylene oxide (PEO). The source of Li ion in the electrolyte solution is electrolyte salts, for example, $LiPF_6$, $LiAsF_6$, $LiClO_4$, which are dissolved in organic solvents. Solvents, such as ethylene carbonate (EC), dimethyl carbonate (DMC), or diethyl carbonate (DEC), are often used in lithium ion batteries. The choice of electrolyte salt and solvent is very important to the performance of a lithium ion battery. The major considerations are the following:

For electrolyte salts:

- High degree of dissociation in solution.
- Thermal and electrochemical stability.
- Safety, non-toxicity and low cost.

For solvents:

- Stability towards electrodes (both cathode and anode).
- Safety, non-toxicity and low cost.

1.5 Mechanism of SEI formation

Unfortunately, most electrolyte solvents, (e.g. ethylene carbonate (EC), dim ethyl carbonate (DMC) or diethyl carbonate (DEC)) presently used in lithium ion battery, are thermodynamically unstable at operating voltages of 3.5 to 4.5 V [24, 25, 26]. Under this high voltage, films due to reduction and oxidation or decomposition of electrolyte and solvent, also called the solid electrolyte interphase (SEI), are expected to form on the surface of both graphite based anodes and active lithium transition metal oxide cathode .These SEI films can lead to irreversible loss of electro active material and electrolyte, thus deteriorating battery performance. For example, an SEI film cause a substantial reduction in energy density, a higher kinetic barrier, poor cyclability and self discharge [27, 28]. However, the SEI also protects the electrode surface from further reaction and provides an ionically conductive interface between electrode and electrolyte for the Li^+ ions. Thus SEI properties are vital to overall battery performance. The major differences between SEI formation on the anode and cathode result from the

different chemical reaction. The composition and structure of the SEI is complex, but it generally depends on the types of solvent or solvent mixture and electrolyte salts that are used in the battery.

Much attention has been devoted in recent years to exploring the function and formation mechanism of SEI films on graphite based anodes, although the properties and structure of the SEI film on such anodes is still unclear [29, 30, 31]. In particular, in situ scanning tunneling microscopy (STM) and atomic force microscopy (AFM) were carried out to observe the SEI formation process, and revealed that the SEI film at the anode is formed at potentials more negative than 0.7 V versus Li/Li^+ [32, 33]. Aurbach et al, proposed a mechanism of electrolyte decomposition based on the analysis of the basic chemistry of the SEI film on graphite based anode surface. Anderson et al, studied the thermal stability and production of decomposition of the SEI by differential scanning calorimetry (DSC) and x-ray photoelectron spectroscopy (XPS), and proposed several different reaction schemes. Peled et al, used various techniques to study the formation of SEI film on the basal plane and cross section of highly oriented pyrolytic graphite (HOPG) in $LiAsF_6$ with EC and DEC electrolyte system, and concluded that the SEI film is thinner on the basal plane than on edge site.

More recently, studies conducted by our research group provide experimental evidence of the existence of SEI on both cathode and anode surface using solid state NMR technique. In addition, our research group performed a very detailed solid state NMR study of intercalated versus non-intercalated lithium in order to provide an understanding of SEI formation on both anode and cathode [33, 34].

1.6 Motivation and objectives

The recent growth of the commercial market in rechargeable lithium ion battery is very remarkable. The driving force for the researcher comes not only from the huge market but also from fundamental science understanding of process of lithium ion transport. In this work we propose to apply fundamental NMR techniques to the characterization of one of the most important irreversible chemical reactions that occur in lithium ion batteries: SEI formation.

Chapter 2 Principles of nuclear magnetic resonance

The experimental technique of nuclear magnetic resonance (NMR) is widely used in structural chemistry and solid state studies [1]. In particular, over the last decades, solid state NMR spectroscopy has grown into an indispensable tool for chemical analysis, structure determination, and the study of dynamics in organic, inorganic and biological systems. This chapter outlines: 2.1) simple NMR theory; 2.2) important interactions in solid state NMR; 2.3) solid state NMR experimental method; and 2.4) data processing in NMR.

2.1 Simple NMR theory

Many review articles and books have been dedicated to the theory and experimental techniques of NMR [2, 3, 4, 5, 6, 7, 8, 9, 10].

Considering a nuclear magnetic moment μ in a homogeneous magnetic field H_0, the Hamiltonian for this system is very simple:

$$H = -\mu \cdot \mathbf{H_0} = -\gamma I \hbar H_0$$

where γ is a constant called the gyro magnetic ratio and I is an nuclear spin number. The eigenvalues of this Hamiltonian are given by

$$E = -\gamma m \hbar H_0$$

For a nuclear spin-1/2 system (i.e. I = 1/2), m has the values 1/2 and -1/2. Thus there are two allowed energy states:

$$E(\left|\frac{1}{2}\right\rangle) = -\frac{1}{2}\gamma \hbar H_0$$

$$E(\left|-\frac{1}{2}\right\rangle) = \frac{1}{2}\gamma\hbar H_0$$

Transitions between these two states are allowed, and the transition frequency is given by the Bohr relation:

$$E(\left|-\frac{1}{2}\right\rangle) - E(\left|\frac{1}{2}\right\rangle) = \hbar\omega_0 = \gamma\hbar H_0$$

where $\omega_0 = \gamma H_0$ is called the Larmor frequency.

2.2 Interactions in solid state NMR

The Hamiltonian of system containing unpaired electrons and nuclei with non-zero spins can be written as [6]:

$$H = H_{el} + H_{CF} + H_{LS} + H_{SS} + H_{CS} + H_{HF} + H_{Zn} + H_D + H_Q$$

where H_{el}, H_{CF}, H_{LS}, H_{SS}, H_{HF}, H_{CS}, H_{Zn}, H_D, and H_Q are the electronic Hamiltonian, the crystal field term, the spin-orbit interaction, the spin-spin interaction, the hyperfine interaction, the chemical shift, Zeeman, dipole-dipole and quadrupolar interactions, respectively.

The electronic Hamiltonian, H_{el} is defined as:

$$H_{el} = \sum_i \frac{p_i^2}{2m} - \sum_{i,n} \frac{Z_n e^2}{r_{ni}} + \sum_{i>j} \frac{e^2}{r_{ij}}$$

n is a sum over the nuclei and i and j are sums over the electrons. H_{CF}, the crystal field term, which is from the electrostatic charges of the ions in ionic compounds and from the chemical bonds in covalent compounds, is defined by

$$H = H_{Zn} + H_D + H_{CS} \qquad \text{(NMR)}$$

$$H = H_{Zn} + H_Q \qquad \text{(NQR)}$$

$$H = H_{nuclear} + H_{Zn} + H_Q \qquad \text{(Mossbauer)}$$

Only interactions that contribute to the phenomena observed by solid state NMR will be discussed below.

2.2.1 Zeeman interaction

When a nucleus with nonzero spin is in the presence of a magnetic field, the nuclear energy level is split into 2I+1 energy level, each with energy

$$H_{zn} = -\mu \cdot \mathbf{H_0} = -\gamma m\hbar H_0 = m\omega_0$$

where μ is the magnetic moment, ω_0 is the resonant frequency, and m is the nuclear spin quantum number. The Zeeman term is the main interaction in solid state NMR and the other interactions are usually thought of as perturbation terms. NMR detects the energy transition between two Zeeman levels. Fig. 1 shows Zeeman levels for I = 1/2 and I = 3/2.

2.2.2 Chemical shift interaction

A uniform external magnetic field H_0 applied to a sample of matter induces an electric current. In an insulating diamagnetic material, only the orbital motion of electrons contributes to this current. The induced electronic current is proportional to

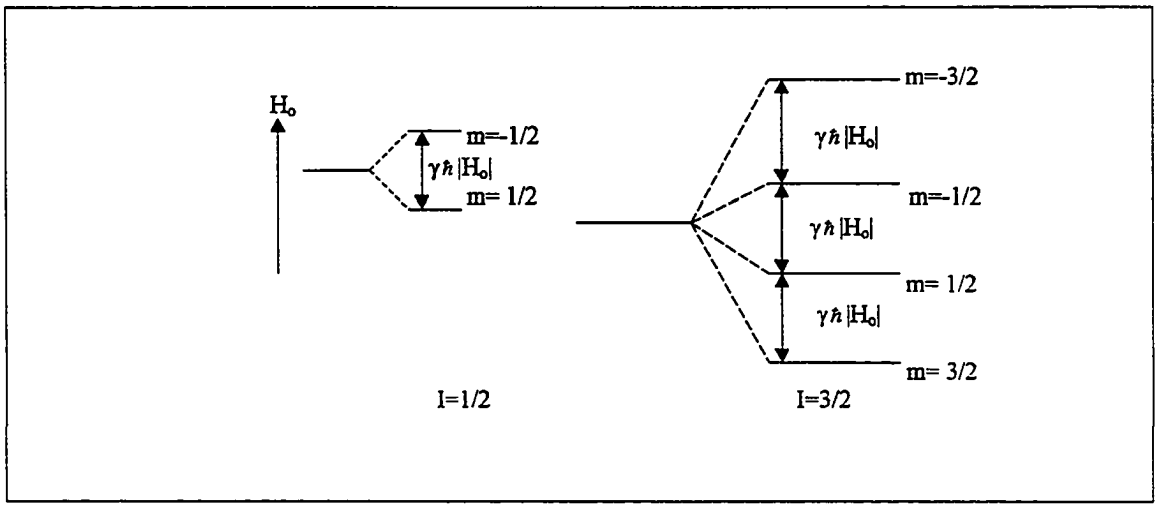

Fig.1.Zeeman energy level for I=1/2 and I=3/2.

the external field H_0, and to first order, is called $\mathbf{j}^{(1)}(r')$. The current $\mathbf{j}^{(1)}(r')$ produces a magnetic field at the nuclear site,

$$H_{in}^{(1)} = \frac{1}{c}\int d^3 r j^{(1)}(r') \times \frac{r - r'}{|r - r'|^3}$$

The chemical shift is defined as the ratio between the induced magnetic field and the external uniform applied magnetic field,

$$H_{in}^{(1)} = - \overrightarrow{\sigma(r)} H_0$$

Here $\overrightarrow{\sigma(r)}$, the chemical shift tensor is orientation dependent. In Cartesian coordinates, $\overrightarrow{\sigma(r)}$ can be transformed to a diagonal tensor by means of the direction cosine matrix R, i.e.,

$$\overline{\sigma(r)}_{diag}=R\,\overline{\sigma(r)}\,R$$

where

$$\overline{\sigma(r)}=\begin{pmatrix}\sigma_{xx} & \sigma_{xy} & \sigma_{xz}\\ \sigma_{yx} & \sigma_{yy} & \sigma_{yz}\\ \sigma_{zx} & \sigma_{zy} & \sigma_{zz}\end{pmatrix}$$

and

$$\overline{\sigma_{diag}(r)}=\begin{pmatrix}\sigma_{11} & 0 & 0\\ 0 & \sigma_{22} & 0\\ 0 & 0 & \sigma_{33}\end{pmatrix}$$

$$R=\begin{pmatrix}\cos\theta_{xx'} & \cos\theta_{xy'} & \cos\theta_{xz'}\\ \cos\theta_{yx'} & \cos\theta_{yy'} & \cos\theta_{yz'}\\ \cos\theta_{zx'} & \cos\theta_{zy'} & \cos\theta_{zz'}\end{pmatrix}$$

Here θ_{ij} $(i=x,y,z\,,j=x',y',z')$ are the angles between the laboratory coordinate system (x,y,z) and principal axis system (x',y',z'). Then the isotropic chemical shift is given by:

$$\sigma_{trace}=\frac{\sigma_{11}+\sigma_{22}+\sigma_{33}}{3}$$

2.2.3 Dipole-dipole interaction

The Hamiltonian for a dipole dipole interaction can be expressed as:

$$H_D = \sum_{i>j} \frac{1}{r_{ij}^3} \overline{I_i D I_j}$$

where r_{ij} is the distance between nuclear spin I_i and I_j, and $\overline{D}$, the dipolar coupling constant tensor, is given by following:

$$\overline{D} = \begin{pmatrix} D_{11} & 0 & 0 \\ 0 & D_{22} & 0 \\ 0 & 0 & D_{33} \end{pmatrix}$$

For two nuclear spin I_1 and I_2, the above Hamiltonian becomes following:

$$H_D = \frac{\gamma_1 \gamma_2 \hbar^2}{r_{12}^3} \left\{ \mathbf{I}_1 \cdot \mathbf{I}_2 - \frac{3(\mathbf{I}_1 \cdot \mathbf{r}_{12})(\mathbf{I}_2 \cdot \mathbf{r}_{12})}{r^2_{12}} \right\} \qquad (1)$$

Rewriting the above Hamiltonian in the spherical coordinate system, with $\mathbf{H_0}$ in the Z direction,

$$H_D = \frac{\gamma_1 \gamma_2 \hbar^2}{r_{12}^3} (A + B + C + D + E + F) \qquad (2)$$

where

$$A = I_{1z} I_{2z} (1 - 3\cos^2\theta)$$

$$B = -\frac{1}{4}(I_1^+ I_2^- + I_1^- I_2^+)(1-3\cos^2\theta)$$

$$C = -\frac{3}{2}(I_{1z} I_2^+ + I_1^+ I_{2z})\sin\theta\cos\theta e^{-i\phi}$$

$$D = -\frac{3}{2}(I_{1z} I_2^- + I_1^- I_{2z})\sin\theta\cos\theta e^{+i\phi}$$

$$E = -\frac{3}{4} I_1^+ I_2^+ \sin^2\theta e^{-i2\phi}$$

$$F = -\frac{3}{4} I_1^- I_2^- \sin^2\theta e^{i2\phi}$$

The frequency shift due to the dipole interaction can be estimated by [11]:

$$\Delta\omega_0 = \frac{\gamma_1\gamma_2\hbar}{r^3_{12}}$$

2.2.4 Quadrupole interaction

The quadrupole interaction Hamiltonian is described by:

$$H_Q = \overline{IQI}$$

where $\overline{Q}$, the quadrupole energy tensor is given by:

$$\overline{Q} = \frac{eQ}{2I(2I-1)\hbar}\overline{V} \quad (\text{or } Q_{ij} = \frac{eQ}{2I(2I-1)\hbar}V_{ij})$$

Q is symmetric and traceless.

$$Q_{ij} = Q_{ji}$$

$$Q_{xx} + Q_{yy} + Q_{zz} = 0$$

The scalar quadrupole moment Q and the gradient of the electric field V_{ij} are defined by:

$$eQ = \int \rho(r) r^2 (3\cos^2\theta - 1) d\tau$$

$$V_{ij} = -\frac{\partial E_i}{\partial x_j} = \frac{\partial^2 V}{\partial x_i \partial x_j}$$

where $\rho(r)$ is the nuclear charge density, and θ is the angle that the radius vector r makes with the internuclear axis. The zz component of the electric field gradient (EFG) is referred to as eq:

$$eq = V_{zz}$$

The asymmetry parameter is defined as:

$$\eta = \frac{V_{xx} - V_{yy}}{V_{zz}}$$

If we assume $|V_{xx}| \le |V_{yy}| \le |V_{zz}|$, then $0 \le \eta \le 1$. In the principal axis system, the Hamiltonian of the electric quadrupole interaction can be written as [4]:

$$H_Q = \frac{e^2 qQ}{4I(2I-1)} \left\{ 3I_z^2 - I(I+1) + \frac{1}{2}\eta (I_+^2 + I_-^2) \right\} \qquad (3)$$

$\frac{e^2 qQ}{\hbar}$ is defined as the quadrupolar coupling constant and $\omega_Q = \frac{3e^2 qQ}{2I(2I-1)\hbar}$ is the quadrupolar coupling frequency. The following first and second order frequency shift can be calculated by perturbation theory,

$$\omega_{m,m-1}^{(1)} - \omega_L = -\frac{\omega_Q}{4}\left[\left(3\cos^2\theta - 1\right) + \eta \sin^2\theta \cos 2\phi \right](2m-1)$$

$$\omega^{(2)}_{-1/2,1/2} - \omega_L = -\frac{\omega_Q^2}{6\omega_L}\left\{I(I+1) - \tfrac{3}{4}\right\}\left\{A(\phi,\eta)\cos^4\theta + B(\phi,\eta)\cos^2\theta + C(\phi,\eta)\right\}$$

where

$$A = -\tfrac{27}{8} - \tfrac{9}{4}\eta\cos 2\phi - \tfrac{3}{8}\eta^2\cos^2 2\phi$$

$$B = +\tfrac{15}{4} - \tfrac{1}{2}\eta^2 + 2\eta\cos 2\phi + \tfrac{3}{4}\eta^2\cos^2 2\phi$$

$$C = -\tfrac{3}{8} + \tfrac{1}{3}\eta^2 + \tfrac{1}{4}\eta\cos 2\phi - \tfrac{3}{8}\eta^2\cos^2 2\phi$$

m is the magnetic quantum number, θ and ϕ are the polar and azimuthal angle, respectively. The η is as defined above.

2.3 Solid state NMR techniques

2.3.1 NMR spectrometer

NMR spectrometers have now become very complex experimental instruments capable of performing many sophisticated and complex experiments. However, the important parts of the spectrometer are not very difficult to understand. The spectrometer consists of the following main components:

Hardware:

- A strong, homogeneous and stable magnetic field.
- Probe which enables the coils used to excite and detect the signal to be placed close to sample.

- A high power RF transmitter capable of delivering short pulses.
- A sensitive receiver to amplify the NMR signals.
- A computer to control everything and process the data.
- Magic angle spinning (MAS) speed controller.
- Temperature controller.

Software:

- A "pulse programmer" to produce pulses at precise times and delays.
- A digitizer to convert the NMR signals into a form which can be stored in computer memory

Fig. 2 shows the schematic of the Chemagnetics CMX-300 spectrometer used in experiment.

2.3.2 Pulse NMR techniques

Most modern NMR measurements are performed in a pulsed mode, i.e. the sample is subjected to short pulses of high-intensity r.f. power and the resulting time dependence of the magnetization is observed along particular directions (usually in the plane perpendicular to the external static magnetic field H_0). The pulses can be varied in terms of frequency, angle with respect to H_0, phase and length, and often the experiments involve a complex sequence of pulses. The effect of these pulses can be considered in classical terms as the motion of precessing magnets of moment μ in magnetic field H_0. The tipping angle θ of M is given by

$$\theta = \gamma H_1 t_p$$

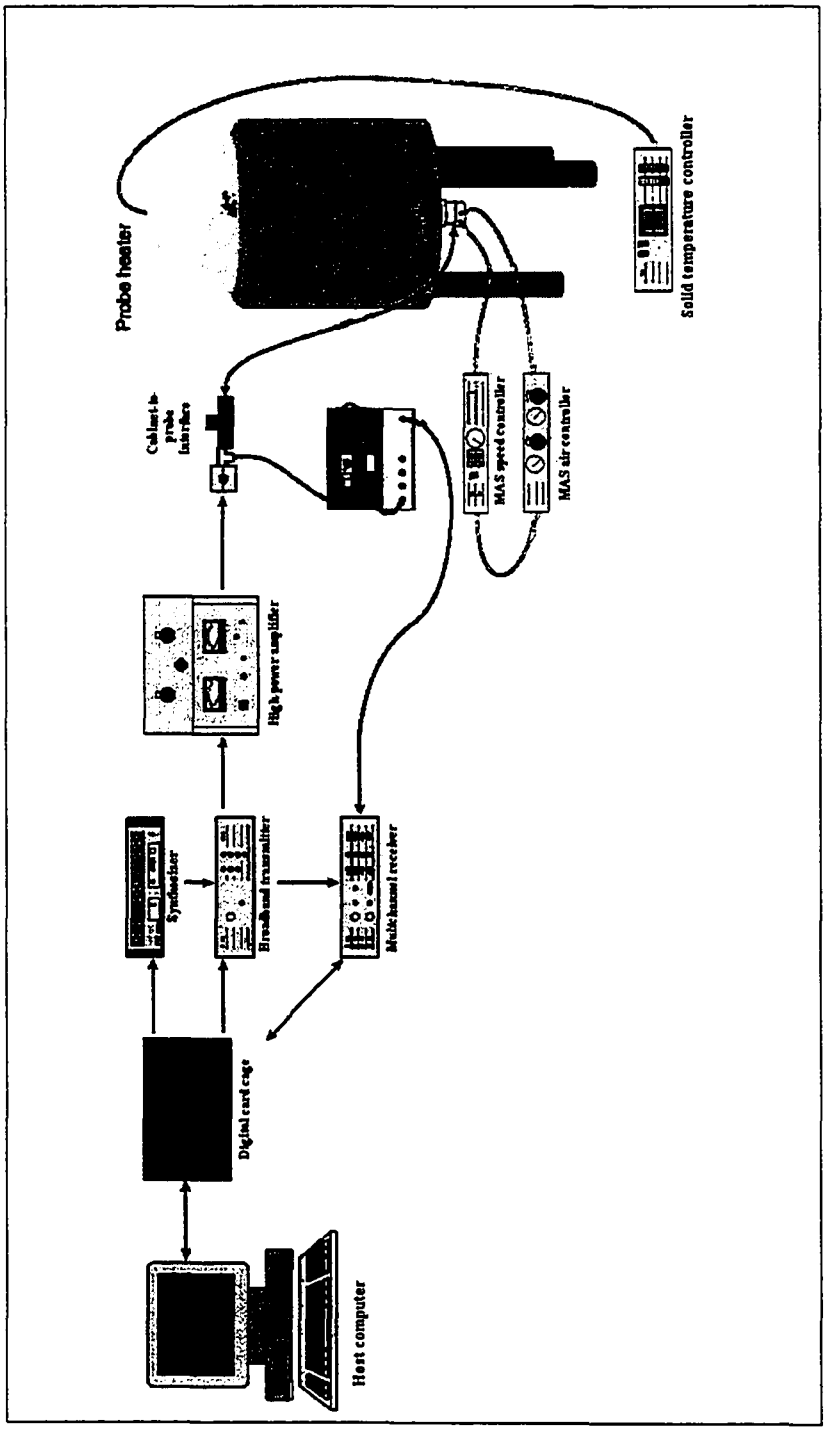

Fig. 2 The schematic of the Chemagnetics CMX-300 spectrometer

where H_1 is the r.f. magnetic field ($|H_1| << |H_0|$), and t_p is the duration of H_1. A basic pulsed experiment is to apply an intense r.f. pulse at resonance to tip the magnetization M 90° from the H_0 direction. This gives rise to a decaying and oscillating magnetization, M_{xy}, in the xy-plane, which can be observed as an induced voltage in a detector coil. M_{xy} will decay with time as the nuclei dephase due to spin-spin interactions and the inhomogeneity of the field H_0 (Fig.3). The decaying signal in the detector coil, proportional to $M_{xy}(t)$, is known as the Free Induction Decay (FID) and the spectral lineshape is its Fourier transform.(Fig. 4)

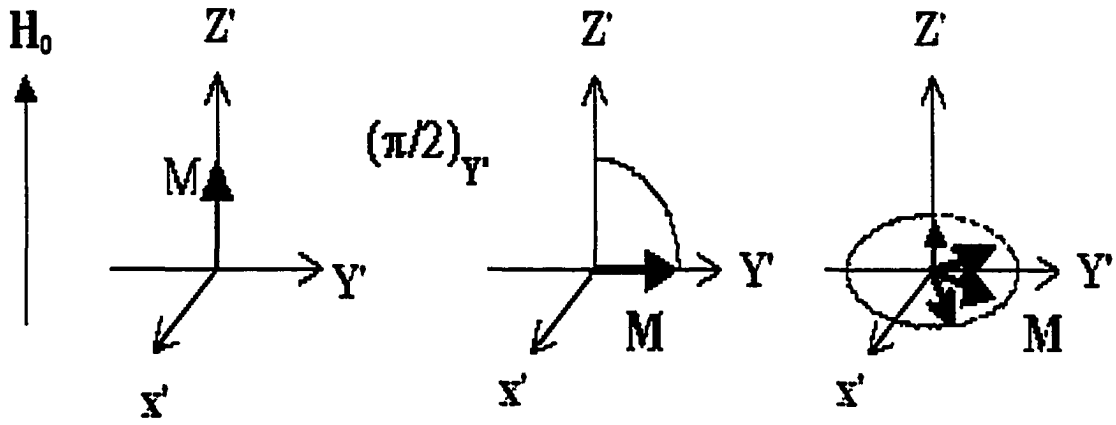

Fig. 3 Effect of R.F. pulse on magnetization M

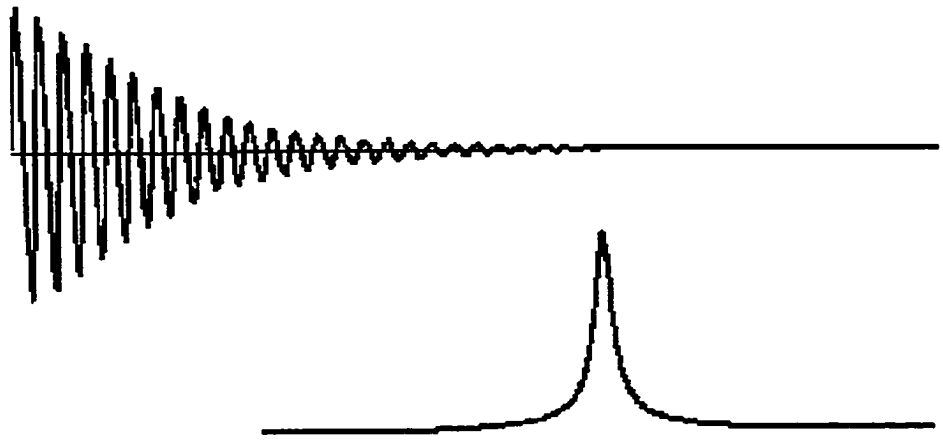

Fig. 4 Free induction decay signal (FID)(top) and corresponding spectrum (bottom)

The time constant for this decay is termed the transverse relaxation time, T_2^*, and is approximately $1/\Delta\omega$. $\Delta\omega$ is the full width at half magnitude or the linewidth of the NMR spectrum.

2.3.3 MAS NMR techniques

The Magic Angle Spinning (MAS) technique is often used to improve the resolution of NMR signals. In the interactions between the nucleus and its environment, dipole-dipole coupling, chemical shift effect and the first order nuclear electrical quadrupole interaction all have an angular dependence given by the Legendre polynomial of the second kind $P_2(\cos\theta)$, where θ is the angle between the magnetic field and an intrinsic axis of the crystal. Rotating the sample rapidly makes the intrinsic axis effectively average out to the rotation axis. When the rotation axis is chosen to be at the magic angle $\theta = 54.74^\circ$, all interactions of the form $(3\cos^2\theta-1)$ will vanish. This technique has been used successfully to reduce the dipolar interactions in a solid but it is only successful when the rate of rotation is rapid compared to the line width for the static spectrum of the sample.

2.4 Data processing [12, 13, 14, 15, 16, 17]

In previous section we discussed how the precessing magnetization can be detected to give a signal which oscillates at the Larmor frequency. This signal, called the free induction decay (FID), will decay due to the action of relaxation. In this section, we will focus on discussing how to change the FID signal, which is in the time domain, into the spectrum in which it is in the frequency domain. This conversion can be carried out by a mathematical process known as Fourier transformation (FT), as is shown in Fig. 4 (top: FID signal, bottom: the spectrum)

If we assume magnetization starts along the x-axis, the component of magnetization based on vector model can be given by:

$$M_x = M_0 \cos \omega t$$

$$M_y = M_0 \sin \omega t$$

where M_0 is determined by instrumental factors. The signal detected is proportional to these magnetizations, so the detected x and y component of signal can be given by

$$F_x(t) = F_0 \cos \omega t$$

$$F_y(t) = F_0 \sin \omega t$$

As a consequence of the characteristics at Fourier transform, it is convenient to take $F_x(t)$ and $F_y(t)$ as the real and imaginary parts of a complex signal and rewrite the above equation as:

$$F(t) = F_x(t) + iF_y(t)$$

$$= F_0 \exp(i\omega t)$$

Considering the transverse magnetization decays over time, this is most simply represented by an exponential decay with a time constant T_2. The signal then becomes:

$$F(t) = F_0 \exp(i\omega t)\exp(-\frac{t}{T_2})$$

where T_2 is the transverse relaxation time. The shorter the time T_2 the more rapidly the signal decays. A typical example is illustrated in Fig. 4(top).

Fourier transformation of a signal such as that given in above equation gives the frequency domain signal which we call as the spectrum, as is shown in Fig. 4 (bottom).

Chapter 3 Solid electrolyte interphase formation in lithium ion batteries

(*EIS has been carried out by our collaborator Dr. Smart of JPL)

The purpose of this chapter is to report on use NMR to study the properties of the solid electrolyte interphase (SEI) formed on both cathode and anode surfaces of lithium ion batteries, as discussed in Chapter 1. The effect of varying the ratio of ethylene carbonate (EC) and dimethyl carbonate (DMC) on the formation of SEI is also discussed. In addition, Electrochemical impedance spectroscopy (EIS) has been carried out to study the effect of aging and high temperature storage on the SEI characteristics of carbon electrodes (mesocarbon microbeads (MCMB) based materials), cathode electrodes, and the subsequent impact on electrode kinetics.

3.1 Introduction

To date, only few studies have been reported on SEI formation on lithium transition metal oxide cathodes. In this work, we focus on the formation of SEI film on $LiNi_{0.8}Co_{0.2}O_2$ cathodes and on MCMB graphite based anodes. $LiNi_{0.8}Co_{0.2}O_2$ active cathode and MCMB graphite based anode, from lithium ion batteries that contains 1 M $LiPF_6$ electrolyte with different ratio of EC and DMC mixture solvent, have been investigated using solid state ^7Li NMR and MAS ^7Li NMR. The changes in the SEI film

on both anode and cathode were also studied. The influence of the ratio of EC to DMC on the SEI was monitored by changes in the intensity of the SEI peak in NMR.

3.2 Experimental

The cells studied in this work were prepared by Dr. Marshall Smart at JPL. They include a MCMB graphite based anode, a $LiNi_{0.8}Co_{0.2}O_2$ cathode and a 1 M $LiPF_6$ electrolyte consisting of EC and DMC. The anode and cathode were removed from charged and discharged lithium ion batteries. The samples studied are summarized in Table 1.

Table 1. Summary of preparation condition of the sample

Sample	Description	Ratio of EC and DMC
Y32A	MCMB anode with 1.0M $LiPF_6$ EC+DMC	70:30
Y34A	MCMB anode with 1.0M $LiPF_6$ EC+DMC	30:70
Y32C	$LiNi_{0.8}Co_{0.2}O_2$ cathode with1.0M $LiPF_6$ EC+DMC	70:30
Y34C	$LiNi_{0.8}Co_{0.2}O_2$ cathode with1.0M $LiPF_6$ EC+DMC	30:70

For the NMR measurements, the anode and cathode materials were scraped off the copper current collector and aluminum screen, respectively. The dried powder was packed into a 5 mm od Pyrex tube and a 3.2mm MAS rotor. All procedures have been performed in an N_2 glove box. Both broad line and high-resolution MAS ^7Li NMR spectra were obtained with a Chemagnetics CMX-300 spectrometer operating at a ^7Li resonance frequency of 116.8 MHz. 1M aqueous LiCl solution was used as a chemical shift reference. A single pulse sequence with pulse width of 3.5 μs and pulse delay of 20.0 s was employed for the anode spectra. For the wide line typical of lithium transition metal oxide cathode, a quadruple echo pulse sequence with a pulse width of 2.5 μs and a single pulse sequence with a pulse width of 2.5 μs and pulse delay of 5 s were performed. Spinning speeds for MAS spectra were 12 and 20 KHz.

3.3 Results and Discussion

3.3.1 The effect of temperature and aging on performance

To study the effect of temperature and aging on the electrochemical performance of lithium ion batteries, the cells were subjected to storage periods of 10 days at increasing temperatures (55, 60, 70 and 75 °C), for a total storage time of 40 days . The cells were stored in open circuit condition in full charge state. The aging characteristic of the cells with different ratio of EC content at various temperatures are shown in Table 2 . As shown in Table 2, the cell which contained electrolytes with high

EC content displayed the greatest resistance to high temperature storage. In contrast, cells with low EC content showed the great irreversible capacity loss after each storage period. Fig. 1 shows results for the cell with low EC content obtained by EIS before and after storage at 55 °C. The discharge capacity of the cell containing electrolyte with high EC content before and after OCV storage at 55 °C is shown in Fig. 2.

Table 2.The aging characteristic of the cells with different ratio of EC content at various temperatures (from Smart et al)

Electrolyte type	Prior to storage	After storage At 55°C		After storage At 55°C +60°C (total 20 days)		After storage At 55°C +60°C +65 °C (total30 days)		After storage At 55°C +60°C +65 °C +70 °C (total 40 days)	
	Ahr	Ahr	%	Ahr	%	Ahr	%	Ahr	%
1.0 M $LiPF_6$ EC/DMC (70/30)	0.298	0.310	104.20	0.304	102.19	0.284	95.44	0.264	88.81
1.0M $LiPF_6$ EC/DMC (30/70)	0.356	0.306	85.97	0.214	60.14	0.114	32.18	0.053	14.93

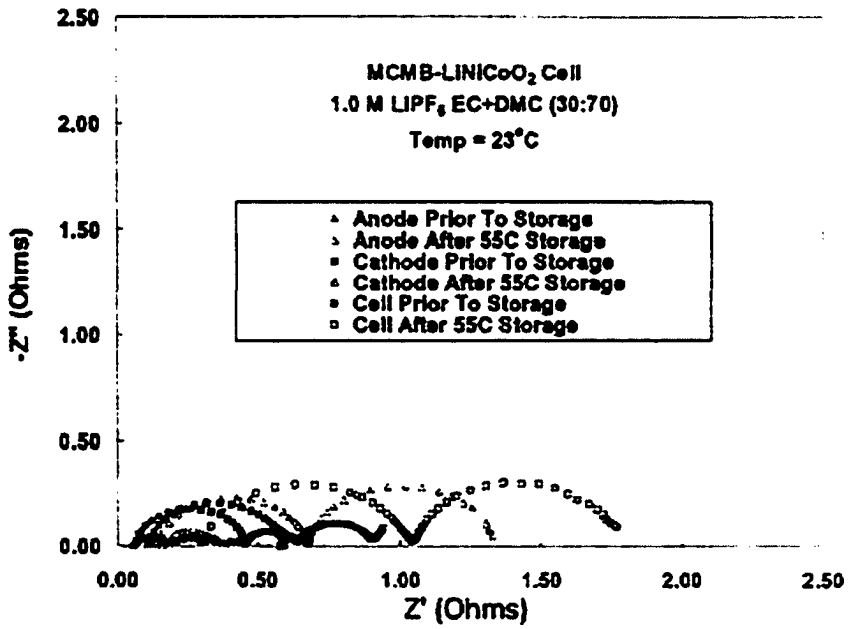

Fig. 1 AC impedance plots of cell containing low EC-content electrolyte before and after storage at 55 °C (Smart et al)

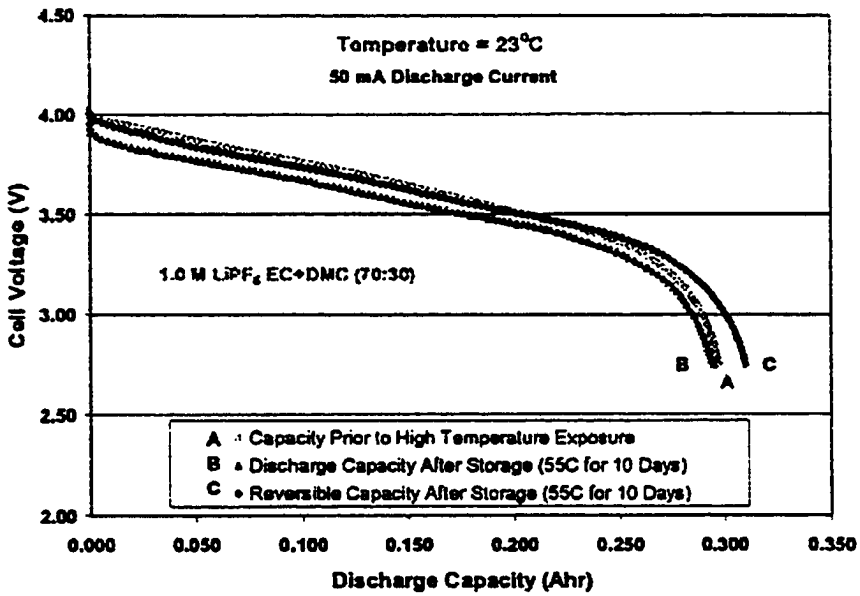

Fig. 2 Discharge capacity of the cell containing electrolyte with high EC content before and after OCV storage at 55 °C (Smart et al)

3.3.2 NMR of aged MCMB graphite anode

Lithium 7 wide line NMR spectra of MCMB graphite based anodes are shown in Fig. 3. It is clear that a single relatively broad line is located at around 15 ppm, and quadrupole satellite transitions are observed. The peak at 15 ppm is attributed to lithium intercalated graphite, as reported in reference [1, 2]. On the other hand, the spectrm of the anode from the EC-rich cell shows a small additional lithium component at 0 ppm from the SEI. This is because lithium compounds inside SEI film are either fully ionized (as in salt) and inactive to the charge or have very small chemical shifts. The spectrum of the DMC rich anode, however, shows a large intensity centered around 0 ppm.

The MCMB graphite based anode materials was also studied by high-resolution MAS ^{7}Li NMR spectroscopy. As shown in Fig. 4, the spectra exhibit several main features: The previously mentioned peak around 15 ppm, which overlaps the SEI component near 0 ppm, and in the case of the DMC-rich anode, there is a small component near 50 ppm. Spinning sidebands are also observed. As mentioned before, the peak at 50 ppm, is assigned to lithium intercalated into MCMB graphite based anode, as a 45 ppm peak is often recognized as the signature of single stage LiC_6[3]. Again, the peak at 0 ppm results from the lithium in the SEI film, therefore, it can be concluded that the SEI film contains highly ionized species with lithium salt-like composition.

Computer simulation of the MCMB spectra will be discussed in section 3.3.4. It is difficult to calculate the reversible and irreversible lithium content in the electrode

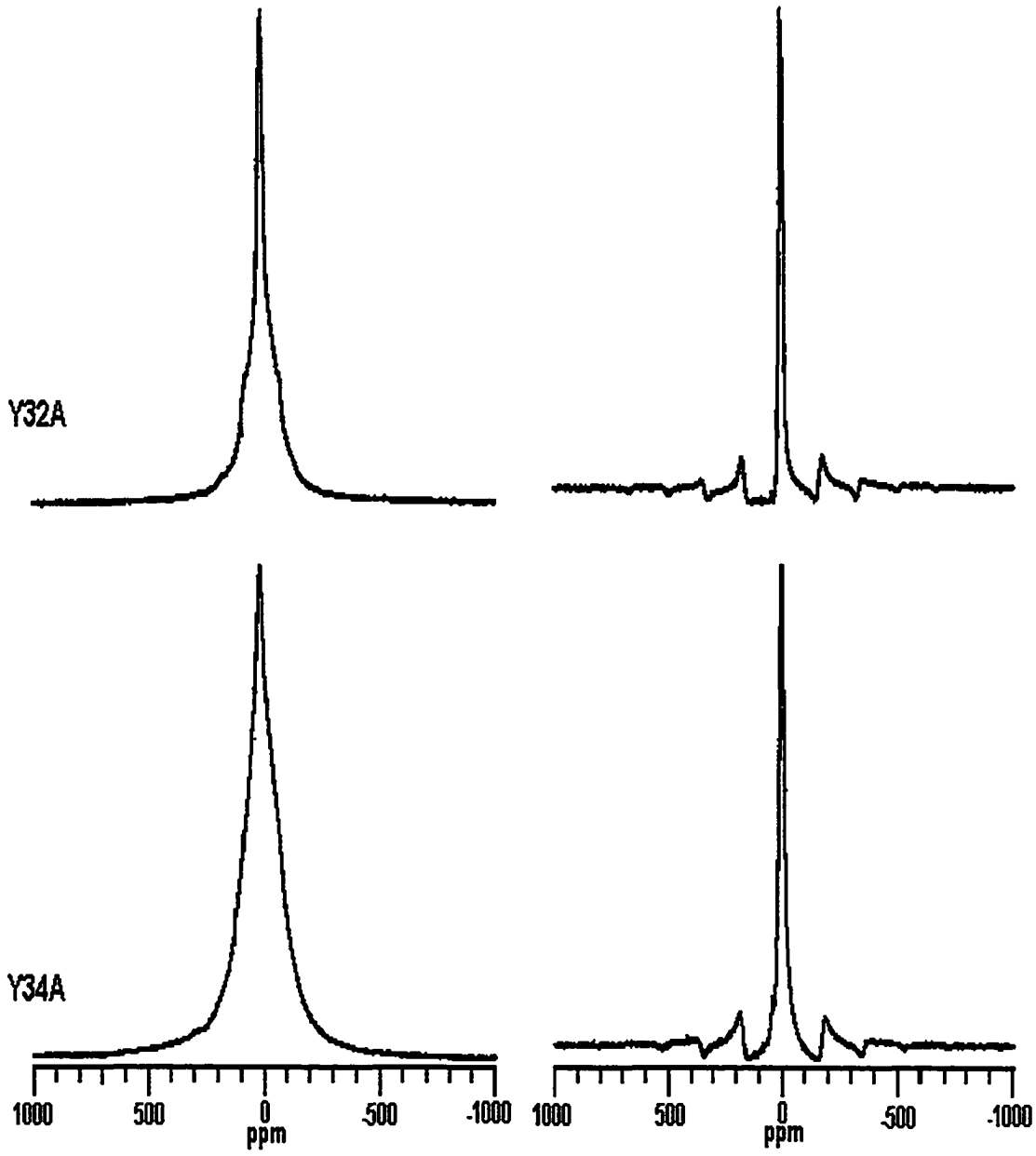

Fig. 3 Wide line ^{7}Li NMR spectra of MCMB graphite anode

Fig. 4 High resolution MAS ^{7}Li NMR spectra of graphite anode (spinning rate 12kHz)

(Y32A: EC / DMC = 70/30, Y34A: EC / DMC = 30/70)

and SEI due to large spectral overlap, but it is clear that the anode from the DMC rich cell has a significantly broader line centered around zero ppm (in both wide-line and MAS). Our preliminary interpretation is that this anode has a larger SEI content than the one from the EC rich cell.

3.3.3 NMR of aged $LiNi_{0.8}Co_{0.2}O_2$ cathode

Fig. 5 shows wide line NMR spectra of a $LiNi_{0.8}Co_{0.2}O_2$ active cathode material. It can be seen that one main peak is located at 164.9 ppm, and another peak at -26.4 ppm. The peak at 164.9 ppm, which has a much smaller chemical shift than that of pure $LiNi_{0.8}Co_{0.2}O_2$ (580 ppm), can be attributed to partially deintercalated $LiNi_{0.8}Co_{0.2}O_2$. It should be noted that there exist different oxidation states of nickel ($Ni^{3+/4+}$) and cobalt ($Co^{3+/4+}$) in the $LiNi_{0.8}Co_{0.2}O_2$ system as a function of charge states. Co^{3+}(electron configuration:t_{2g}^6 e_g^0) and Ni^{4+} are diamagnetic, while Co^{4+} and Ni^{3+}(electron configuration:t_{2g}^6 e_g^1) are paramagnetic. It is easier to oxidize nickel ions than cobalt ions during lithium deintercalation. In case of deintercalated $LiNi_{0.8}Co_{0.2}O_2$, fewer Ni^{3+} ions are present at octahedral sites, having been partially replaced by oxidized Ni^{3+}(i.e Ni^{4+}). Thus, the interaction between lithium ions and the nearest paramagnetic ions is weaker in deintercalated $LiNi_{0.8}Co_{0.2}O_2$ than in pure active $LiNi_{0.8}Co_{0.2}O_2$. Thus the chemical shift of pure active $LiNi_{0.8}Co_{0.2}O_2$ (580 ppm) should be larger than that of deintercalated $LiNi_{0.8}Co_{0.2}O_2$ cathode (164.9 ppm), as we observe, another interesting feature, is the second peak around -26.4 ppm, which is assigned to the SEI on the cathode surface. There is only a small change in relative intensity of this SEI peak as a function of the ratio of EC and DMC in the electrolyte solvent.

In order to determine the site assignment and analyze their relative populations, high resolution MAS ^{7} Li NMR measurement were performed. Fig. 6 shows spectra of MAS ^{7} Li NMR for $LiNi_{0.8}Co_{0.2}O_2$ cathode. As can be seen, the spectrum is complex and extends over a wide range of frequencies of over 800 ppm.

The narrow resonance near -26.4 ppm was assigned to the solvated lithium ions of SEI as before. The central transition resonance in Fig. 6 displays a shift of around 170 ppm, which is associated with the lithium ions in $LiNi_{0.8}Co_{0.2}O_2$ cathode, consistent with the wide line result. The MAS ^{7}Li NMR spectra with two different spinning speeds of 12 and 20 kHz for $LiNi_{0.8}Co_{0.2}O_2$ cathode are given in Fig. 7, in order to distinguish spectral peaks from spinning sidebands.

3.3.4 Computer simulation for ^{7}Li NMR spectra

In this investigation it is important to estimate the reversible and irreversible lithium in the electrodes and the SEI. This can be done by deconvolution and integration of the ^{7}Li NMR peaks. Lineshape simulation was performed using PEAKFIT program (Systat Software Inc). The area of the peaks at -26.4 and 164.9 ppm, which are due to SEI and active cathode in ^{7}Li NMR spectra, are considered to be proportional to the amount of irreversible and reversible lithium, respectively. The simulation shows that the ratio of irreversible to reversible lithium is around 0.13:1 for the cathode with low EC content (EC:DMC = 30:70, sample Y34C), and around 0.17:1 for cathode with EC rich content (EC:DMC = 70:30, sample Y32C). Fig. 8 shows the simulations.

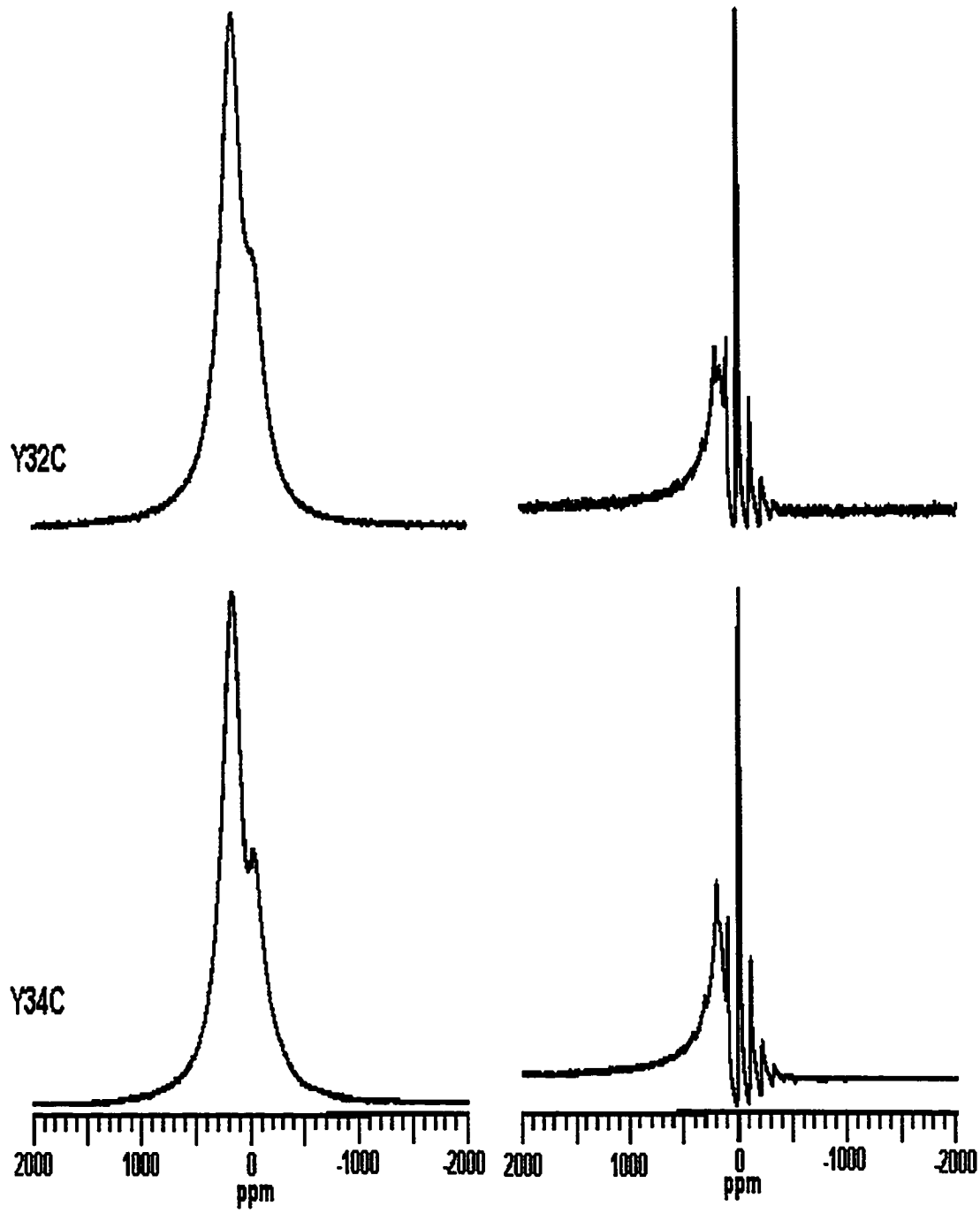

Fig. 5 Wide line ^{7}Li NMR spectra of $LiNi_{0.8}Co_{0.2}O_2$ cathode
cathode

Fig. 6 High resolution MAS ^{7}Li NMR spectra of $LiNi_{0.8}Co_{0.2}O_2$

(spinning rate 12kHz)

(Y32C: EC / DMC = 70/30, Y34C : EC/DMC = 30/70)

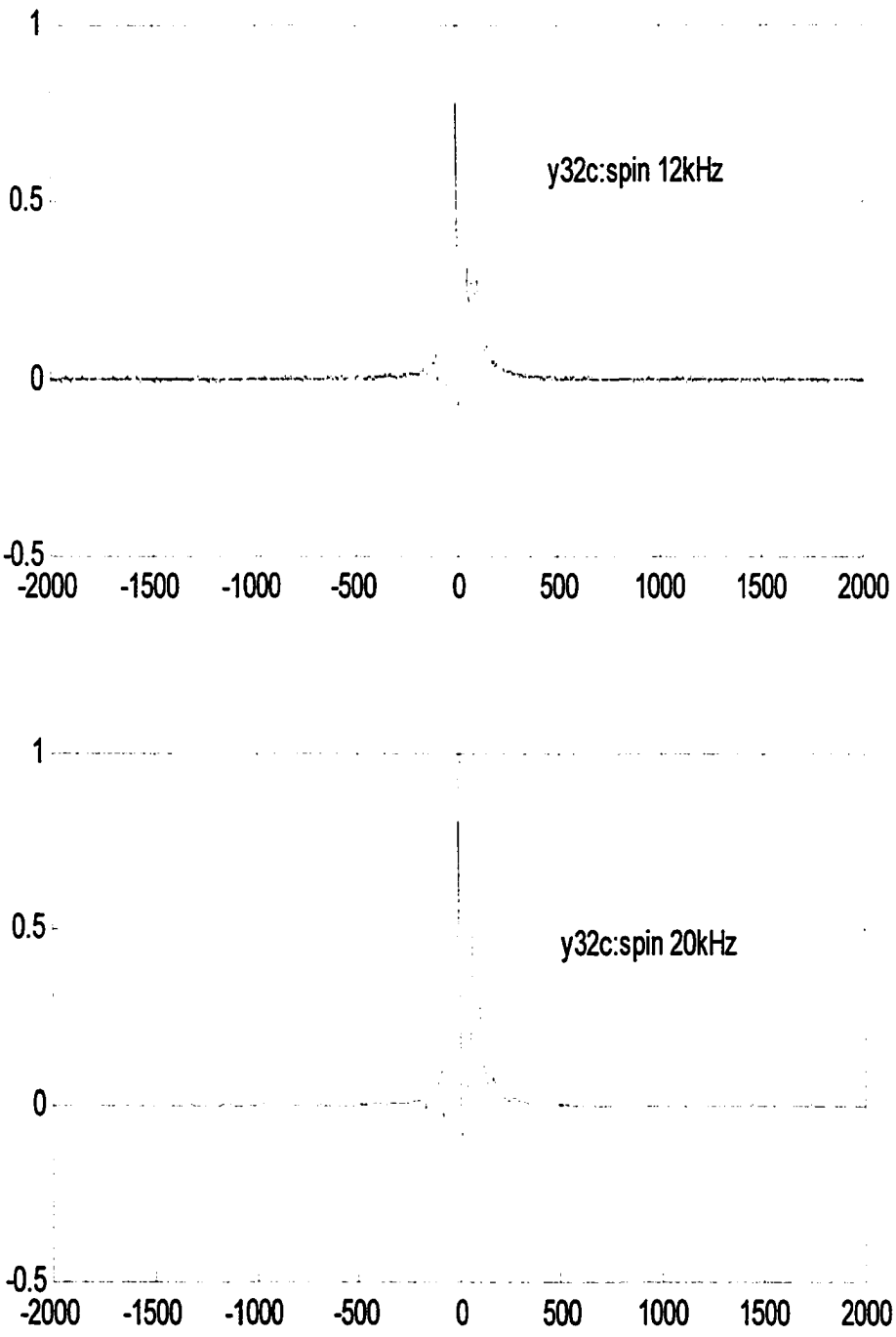

Fig. 7 High resolution MAS ^{7}Li NMR spectra of $LiNi_{0.8}Co_{0.2}O_2$ cathode

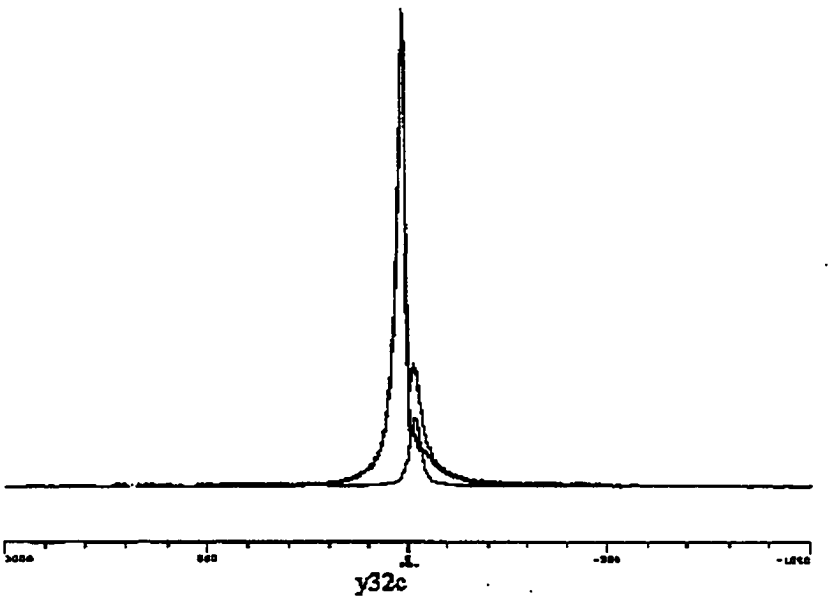

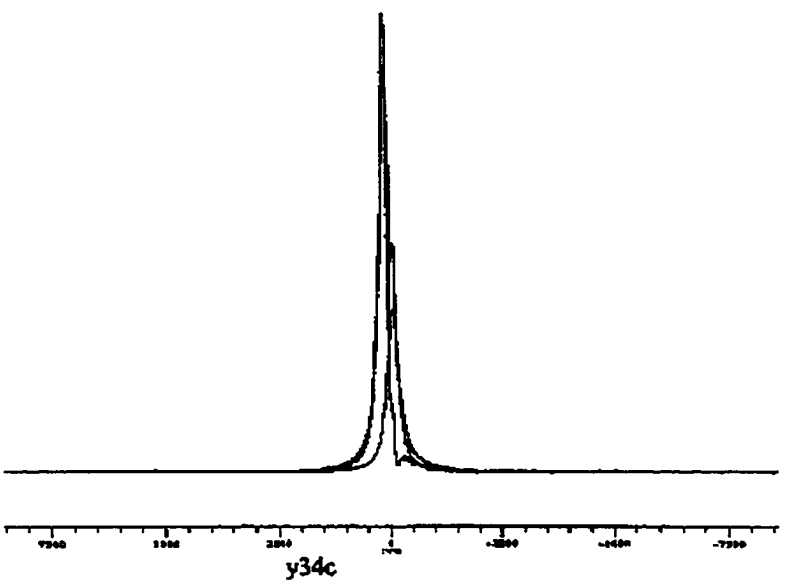

Fig. 8 Simulation for the cathodes

(Y32C: EC / DMC = 70/30, Y34C: EC/DMC = 30/70)

To simulate line shape ^{7}Li NMR spectrum of anode, we have useed the following approach. Generally, there are two kinds of resonance curves of different spectra line shape. One is the Gaussian curve, the other is the Lorentz curve. The former is described by following the normalized function:

$$G(\omega) = \frac{1}{(2\pi)^{1/2}\Delta}\exp(-\frac{(\omega-\omega_0)^2}{2\Delta^2})$$

where Δ is defined as:

$\Delta = \frac{\delta}{(2\log 2)^{1/2}} = \frac{\delta}{1.18}$, and δ is the half width at half height, ω is frequency, ω_0 is resonance frequency. The Lorentzian is described by the normalized function:

$$L(\omega) = \frac{\delta}{\pi[\delta^2 + (\omega-\omega_0)^2]}$$

and $T_2 = \frac{1}{\delta}$.

where T_2 is the transverse relaxation time. This means that the faster the decay of the FID signal the broader the spectrum line shape.

A trial model that describes the spectral shape of the NMR of spectrum is given by the following equation:

$$F(\omega) = pG(\omega) + (1-p)L(\omega)$$

where $0 \le p \le 1$.

We simulate the Li^7 NMR spectrum of anodes based on this model. Fig. 9 shows the results of the simulation for the anode using the Matlab program.

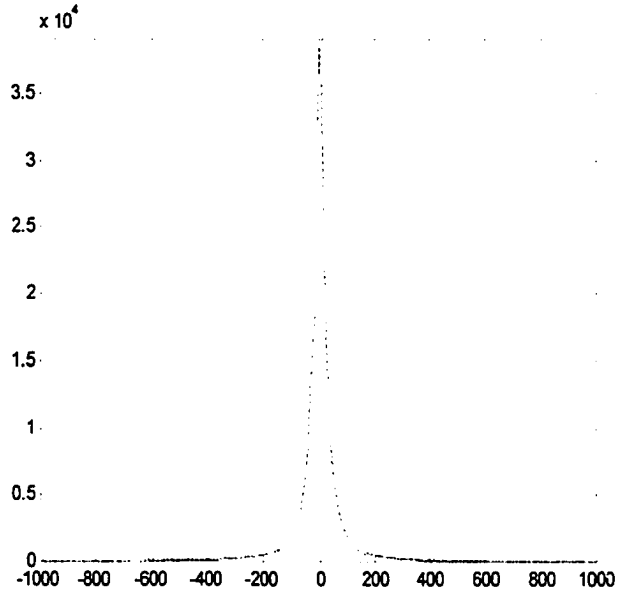

(Y32A)

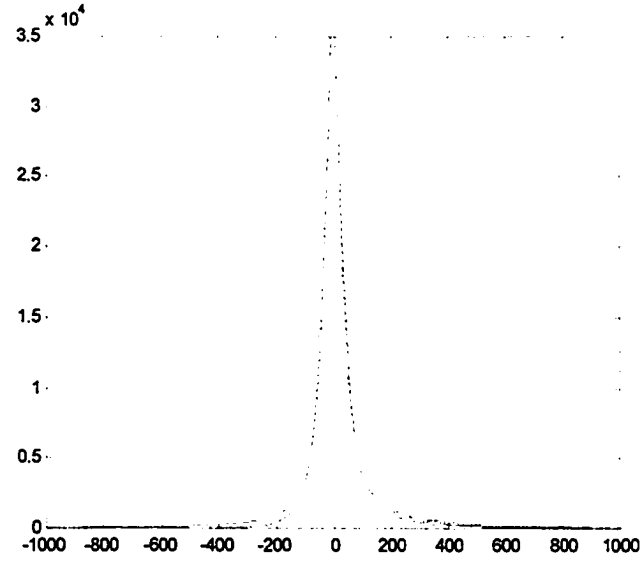

(Y34A)

Fig. 9 The simulation for the anode (dotted line: simulation, solid line: experimental)

(Y32A: EC / DMC = 70/30, Y34A : EC/DMC = 30/70)

3.4. Conclusions

Based on the ^{7}Li NMR and MAS ^{7}Li NMR results, the following conclusion can be drawn:

1) The solid electrolyte interphase is formed not only on MCMB graphite based anode, but also on the $LiNi_{0.8}Co_{0.2}O_2$ cathode.
2) The chemical shift (164.9 ppm) measured in $Li_xNi0_{.8}Co_{0.2}O_2$ cathode is less than that (580 ppm) in pure $LiNi_{0.8}Co_{0.2}O_2$ due to intercalation and deintercalation.
3) In this work, we have determined the effect of the ratio of EC to DMC on the intensity of SEI. We find that a lower EC/DMC ratio is associated with a smaller SEI intensity for the cathode and higher intensity for the anode.
4) The EIS results suggest that the nature of the electrolyte, the electrolyte solvent content and the character of the SEI formed on electrodes play a great role in determining the ability of lithium ion cells to withstand high temperature exposure periods without substantial irreversible capacity loss.

Chapter 4 The effect of temperature on the solid electrolyte interphase in lithium ion battery

The solid electrolyte interphase (SEI) on the surface of $LiNi_{0.8}Co_{0.2}O_2$ cathodes and mesocarbon microbeads (MCMB) graphite anode has been studied using ^7Li nuclear magnetic resonance (NMR) as function of temperature. The temperature dependence of the spin lattice relaxation time is well described by the Bloembergen-Purcell-Pound (BPP) relaxation model over a wide temperature range. An activation energy E_a of 0.47 eV for sample B and 1.67 eV for sample A was obtained from the slope of the $-\ln T_1$ as a function of temperature.

4.1 Introduction

The effect of temperature on the performance and cycling stability of lithium ion batteries has been the object of several studies, since elevated temperature is a very important safety issue in many portable electronics devices [1, 2, 3, 4]. Elevated temperature also affects the performance of lithium ion batteries. Several recent studies have shown that elevated temperature might lead to both dissolution and decomposition of the SEI film and to the formation of additional components [5, 6]. In addition, elevated temperature also accelerated the degradation of battery materials [7, 8]. In contrast, at low temperature, lithium ion batteries exhibit poor performance because the electrolyte solution may become gel-like or even freeze solid. Thus, how to improve low temperature performance is an important issue.

In this work, we study the formation of SEI film on interface of cathode/anode and electrolyte by solid state ^{7}Li NMR techniques. The temperature dependence of the line shape and the line width of the ^{7}Li NMR spectrum at the cathode and the anode are investigated over a wide temperature range.

4.2. Experimental

The samples studied were provided by JPL, and the configuration of the batteries is as follows:

$LiNi_{0.8}Co_{0.2}O_2$ (+)(sample A)|1 M $LiPF_6$ with EC/DMC=30/70|graphite (-) (sample D)

$LiNi_{0.8}Co_{0.2}O_2$ (+) (sample B)|1 M $LiPF_6$ with EC/DMC=70/30|graphite (-)(sample C)

The lithium environment in the cathodes and anodes was studied using solid state NMR, a very sensitive tool to analyze the local environment, particularly in the presence of magnetic cations. The details of NMR measurements have been described in Chapter 3. The spin lattice relaxation time was measured by the inversion recovery method at different temperatures. It should be noted that the recovery magnetization shows a monoexponential behavior. T_1 values were obtained at each temperature using the following function:

$$M(\tau) = M_0[1 - 2\alpha \exp(-\tau / T_1)]$$

to fit the experimental magnetization. Here T_1 is the spin lattice relaxation time, M_0 is the thermal equilibrium magnetization, and α is a fitting parameter.

4.3. Results and discussion

4.3.1 $LiNi_{0.8}Co_{0.2}O_2$ cathode

The ^7Li NMR spectra of the $LiNi_{0.8}Co_{0.2}O_2$ cathode were measured in the temperature range of 173 to 393 K. The spectrum exhibit two peaks for sample A and sample B at room temperature (293 K). As shown in Fig. 1, one peak is centered at around -26.4 ppm, and the other at around 164.9 ppm. The former peak is usually assigned to SEI, while the latter is due to a charged or discharged $LiNi_{0.8}Co_{0.2}O_2$ cathode. This confirms that the chemical environment of Li^+ ions in SEI is different from that in the $LiNi_{0.8}Co_{0.2}O_2$ cathode. However, the peak at 164.9 ppm broadens and shifts further to high field as the temperature decreases. This broadening and chemical shift is due to the increase in the magnetic dipole moment and magnetic susceptibility of Ni^{+3} ions. At low temperature, the magnetic behavior is dominated by the fluctuation of Ni^{3+} spin (S=1/2) due to the super transferred hyperfine interaction via Li (1s)-O (2s)-Ni (3d) bonds. Diamagnetic Ni^{4+} ions in the Ni layer will reduce intra and inter layer interactions between ferromagnetic Ni^{3+} ions [9].

The temperature dependence of full width at half height (FWHH) of the ^7Li NMR spectrum provide an accurate analytical tool for the study of phase separation at elevated temperature. Fig. 2 shows the dependence of the line width over the temperature range of 173 to 393 K for sample A and B, two cathode materials as described on p. 50. As shown in Fig. 2, the line width narrows significantly at high temperature.

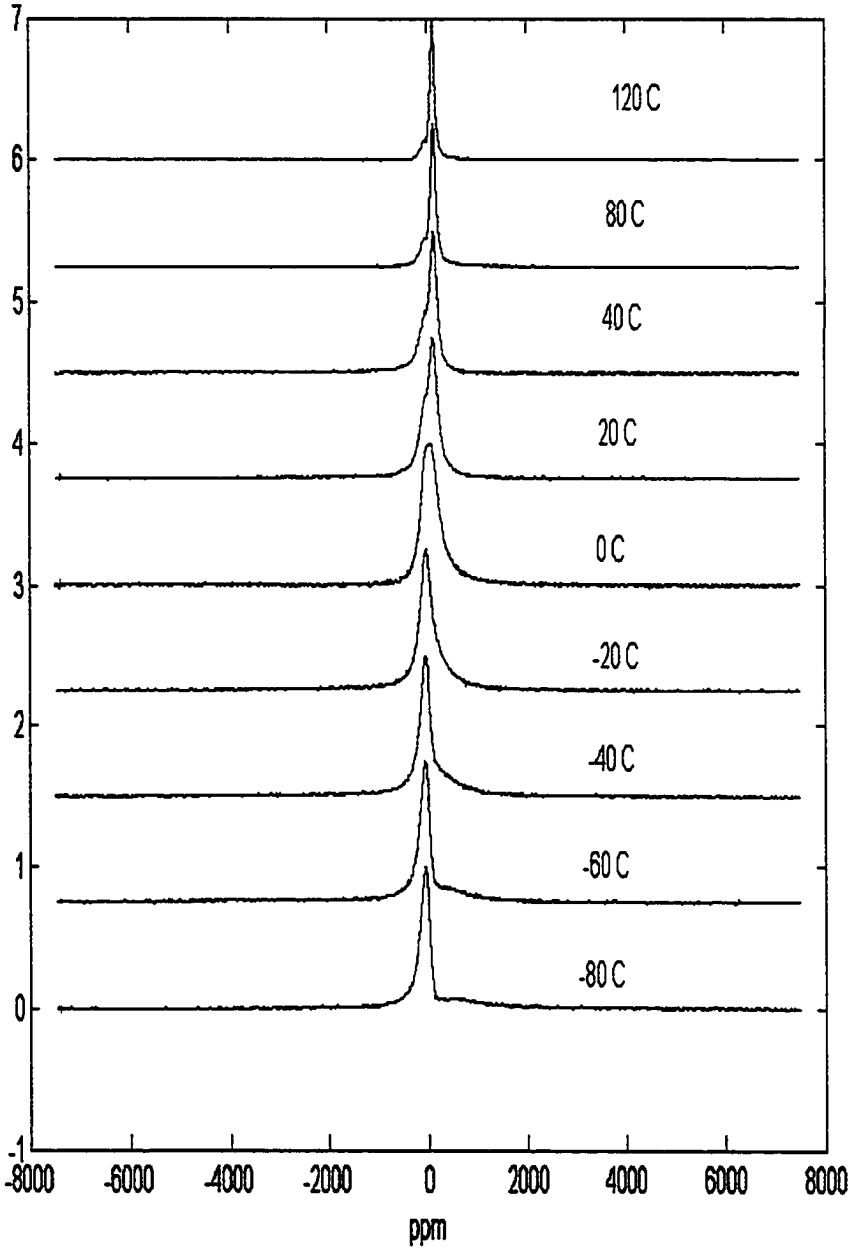

a: (sample A : $LiNi_{0.8}Co_{0.2}O_2$ cathode in EC:DMC = 30/70)

Fig. 1 Static ^7Li NMR spectra of sample A and B at various temperatures

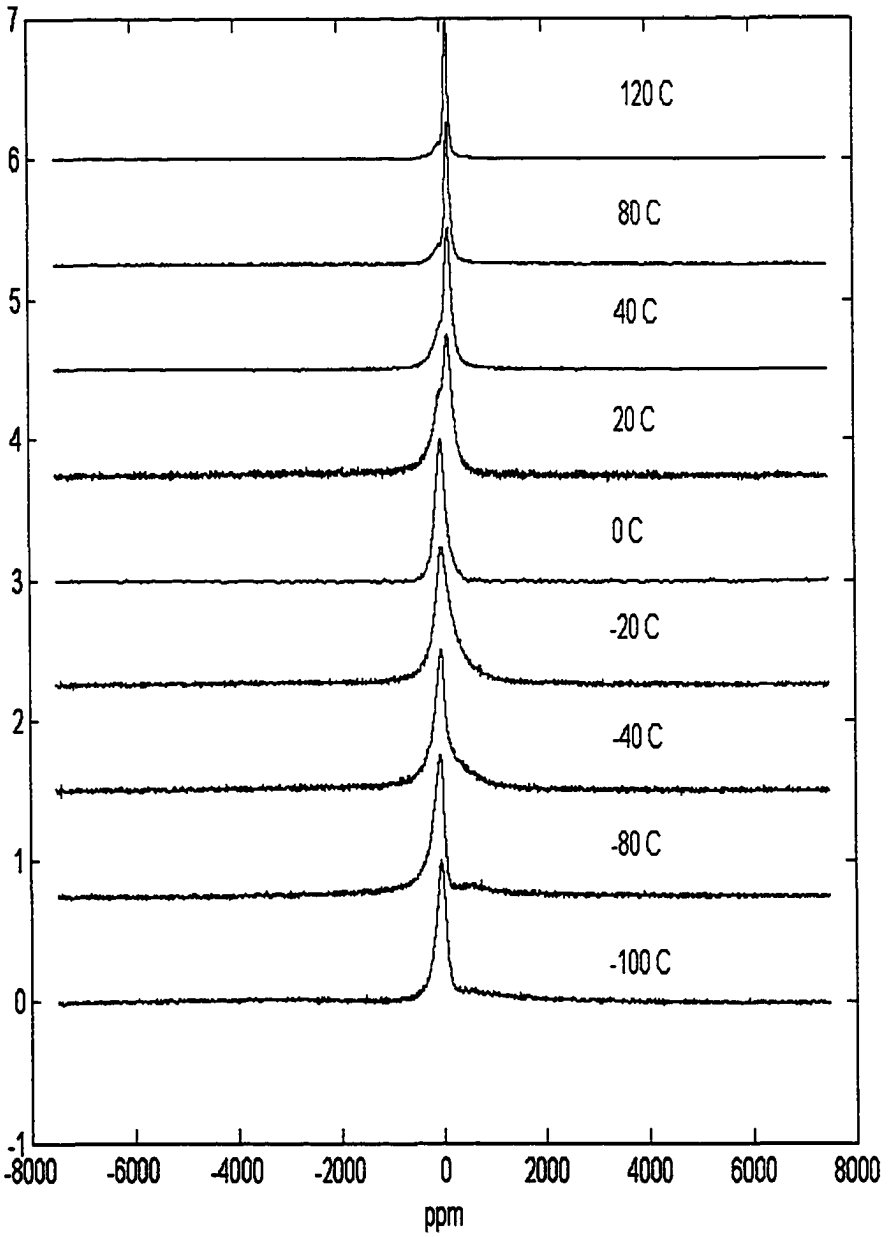

b: sample B

Fig. 1 Cont'd

(sample B: $LiNi_{0.8}Co_{0.2}O_2$ cathode in EC / DMC = 70/30,)

This narrowing may be due to diffusive motion of the lithium ion itself or its nearest neighbors. Note that most of the increase in line width occurs with increasing temperature in the range of 250 to 310 K (-20 to 40 °C), which is the typical temperature range of summer and winter in most places on earth. The line width reaches a maximum at around 250 K for sample A, and 277 K for sample B, below that temperature, the line width decreases with decreasing temperature.

4.3.2 Spin lattice relaxation

In both the cathode and anode, the main contribution to the spin lattice relaxation rate of lithium nuclei, $1/T_1$,

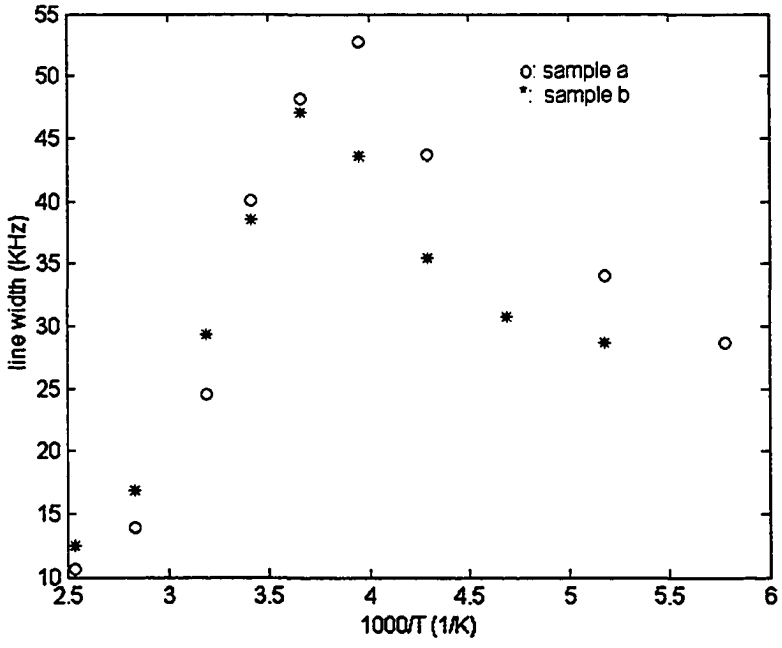

Fig. 2 ^{7}Li NMR line width as a function of temperature for $LiNi_{0.8}Co_{0.2}O_2$ cathode.(*:sample b)and (o:sample a) (sample A : EC:DMC = 30/70, sample B: EC / DMC = 70/30,)

are the following: 1) direct Fermi contact interaction of nuclei with the conduction electrons; 2) the 2s orbital; 3) the nuclear dipole interaction originating from the coupling neighboring lithium nuclei; 4) the quadruple interaction from the coupling of quadruple moment; 5) indirect interaction between lithium nuclei and the neighboring paramagnetic transition metal nuclei. The spin lattice relaxation time for the cathode $LiNi_{0.8}Co_{0.2}O_2$ electrode and MCMB graphite based anode is summarized in Table 1.

Table 1. Summary of spin lattice relaxation time

Sample	Spin lattice relaxation time	
	Main peak (sec.)	SEI peak (sec.)
A	0.0124	0.027
B	0.0129	0.0344
C	2.476	
D	1.394	

It can be seen that the spin lattice relaxation time in the bulk of $LiNi_{0.8}Co_{0.2}O_2$ cathode is shorter than that of its accompanying SEI. This indicates once again that the lithium environment is quite different in these locations. The longer relaxation time in

SEI confirms that this structure is more salt-like than the deintercalated and intercalated cathode.

In addition, we proceed to explain the difference in T_1 observed in cathode and in SEI using the structural point of view and quantum theory. $LiNi_{0.8}Co_{0.2}O_2$, a layered structure cathode compound, can be described as an ordered rock salt structure with lithium and nickel or cobalt ions in the (1 1 1) plane formed from two oxygen fcc packing unit cells. That is, the oxygen ions adopt a cubic closed-packed arrangement with $Ni^{3+/4+}$ or $Co^{3+/4+}$ ions occupying octahedral sites between adjacent oxygen ion layers, the Li^+ intercalated in octahedral positions in the interlayer space [10, 11]. As stated above, low spin Co^{3+} (t_{2g}^6 e_g^0) and Ni^{3+} (t_{2g}^6 e_g^1) are diamagnetic and paramagnetic, respectively, The paramagnetic ions allow the ^7Li to relax more quickly. On the other hand, the SEI does not contain any paramagnetic transition metal ions, so ^7Li relax more slowly, gives rise to the observed longer relaxation time.

One can obtain the following spin lattice relaxation rate equation from quantum theory, based on this mechanism of spin lattice relaxation.

$$\frac{1}{T_1} = R_s^{Fc} + \sum_{i=0}^{N} \sum_{x} \sum_{y} R_x^{y} + o(0) \qquad (1)$$

where N is the number of nearest paramagnetic ions, x stands for p and d components, y for the orbital and dipolar hyperfine interaction, and $o(0)$ represents higher order non-localized interactions, which can be neglected. The R_s^{Fc} and R_x^{y} are given by:

$$R_s^{Fc} = C[H_s^{Fc}.D_s(E_f)]^2 \qquad (2)$$

$$R_x^{\ y} = C[H_x^{\ y}.D_x(E_f)]^2.F_x^{\ y} \qquad (3)$$

with $C = 4\pi\hbar\gamma_n^{\ 2}k_BT$. Here γ_n is the gyromagnetic ratio of the nucleus, k_B the Boltzmann consta fields, which can be calculated using different methods. $F_x^{\ y}$ is a factor related to the crystal nt, and T the temperature. H_s^{Fc} and $H_x^{\ y}$ are the Fermi contact and polarization hyperfine structure. For SEI, the second and third terms in Equation (1) are zero due to the absence of paramagnetic ions so that

$$(\frac{1}{T_1})_{SEI} < (\frac{1}{T_1})_{cathode} \qquad (4)$$

That is, T_1 in the SEI is larger than T_1 in the cathode, as observed.

The temperature dependence of the ^{7}Li spin lattice relaxation time (T_1) for sample A and B are shown in Fig. 3. In both cases, there is an asymmetric temperature dependence of spin lattice relaxation time. A T_1 minimum appears at around 294 K for sample A and 317 K for sample B, respectively. The T_1 minimum is associated with electric dipolar reorientation. On the other hand, it can be seen from Fig. 3 that a similar minimum in relaxation time for two samples is due to the same relaxation mechanism. The explanation is presented elsewhere [10]. The values of ln T_1 for ^{7}Li in sample B exceed the corresponding values in sample A for cathode in temperature range of 173 to 393 K. The relaxation time for ^{7}Li in sample A and B increases progressively with increasing temperature in the range of 294 to 393 K. Relaxation is mainly dominated by the motion of the Li^+. The temperature dependence of the spin lattice relaxation time in

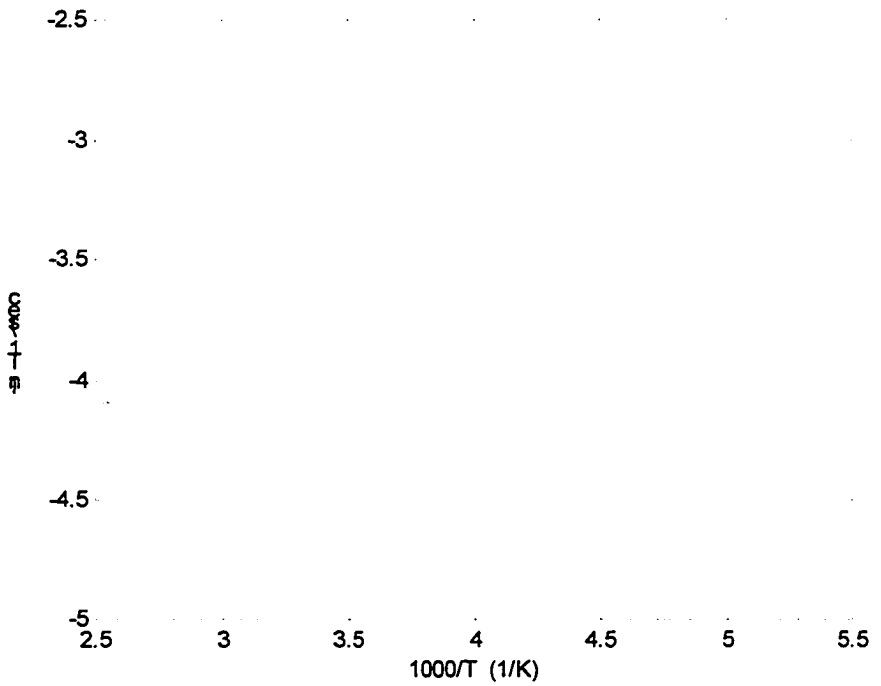

Fig. 3 ln T_1 vs temperature for sample A (o) and B(x)

(sample A : EC:DMC = 30/70, sample B: EC / DMC = 70/30)

the high temperature region can be described by the Bloembergen-Purcell-Pound (BPP) expression:[11]

$$T_1 = C\left(\frac{\tau}{1+(\omega\tau)^2} + \frac{4\tau}{1+4(\omega\tau)^2}\right) \qquad (5)$$

where $\tau = \tau_0 \exp(E_a / kT)$ is correlation time, E_a is the activation energy for Li^+ motion,

and C depends on the mechanism of spin lattice relaxation. It should be noted that this expression follows from Li^+ motion described by the correlation function:

$$\phi(t) = \exp(-t/\tau)^{\beta} \qquad (6)$$

where $\beta = 1$ for this case.

Furthermore, the mean correlation time τ of 8.5×10^{-10} s for the order parameter fluctuation and the activation energy E_a of 0.47 eV for sample B and 1.67 eV for sample A can be calculated by $\omega_l.\tau=1$ and the slope of the ln T_1 vs 1000/T curve in Fig. 3 in the high temperature range.

4.3.3 MCMB graphite Anode

^{7}Li NMR spectra of MCMB graphite anodes under various temperatures are shown in Fig. 4. Two sets of spectra are displayed for each of the two samples, the MCMB graphite with 1 M $LiPF_6$ electrolyte in EC/DMC = 70/30 (sample C) and EC/DMC = 30/70 (sample D). These spectra are dominated by a single relatively broad line from the -1/2 <-> 1/2 transition centered at around 15 ppm. In addition, there is a small additional lithium component at 0 ppm from SEI that overlays with the peak centered at 15 ppm. Quadrupole satellite transitions are observed as weak shoulder on both sides of the main peak from Fig. 4. On the other hand, there is no evidence of reversible intercalated Li species, which would be characterized by Knight shifts of around 40 to 50 ppm. We have previously shown by MAS ^{7}Li NMR that a peak centered at 49.8 ppm, associated with reversible lithium intercalated into MCMB graphite anode, is present, though not well resolved [10].

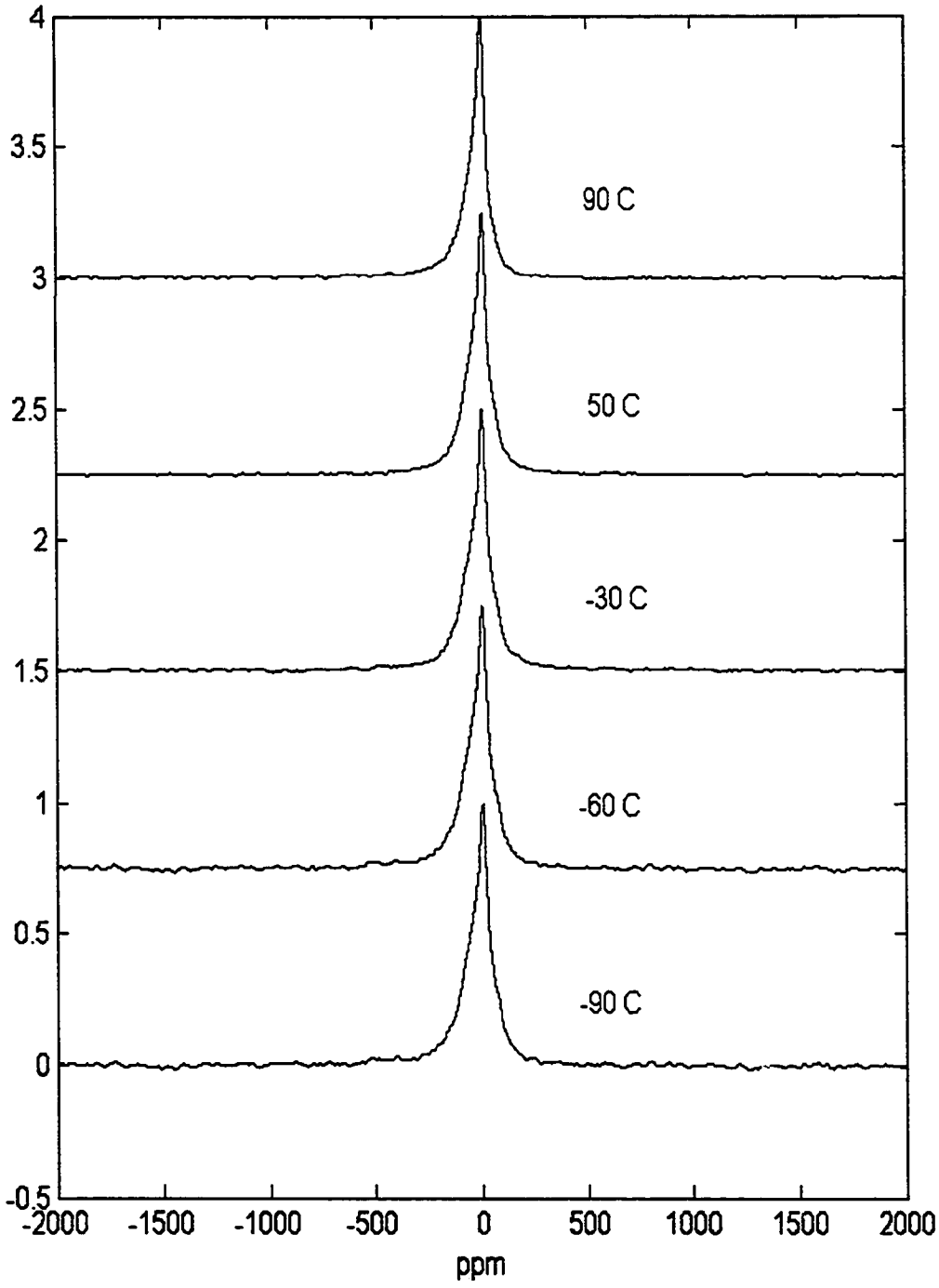

a: sample C

Fig. 4 Temperature dependence of ^{7}Li NMR spectra of sample C (a) and D (b)

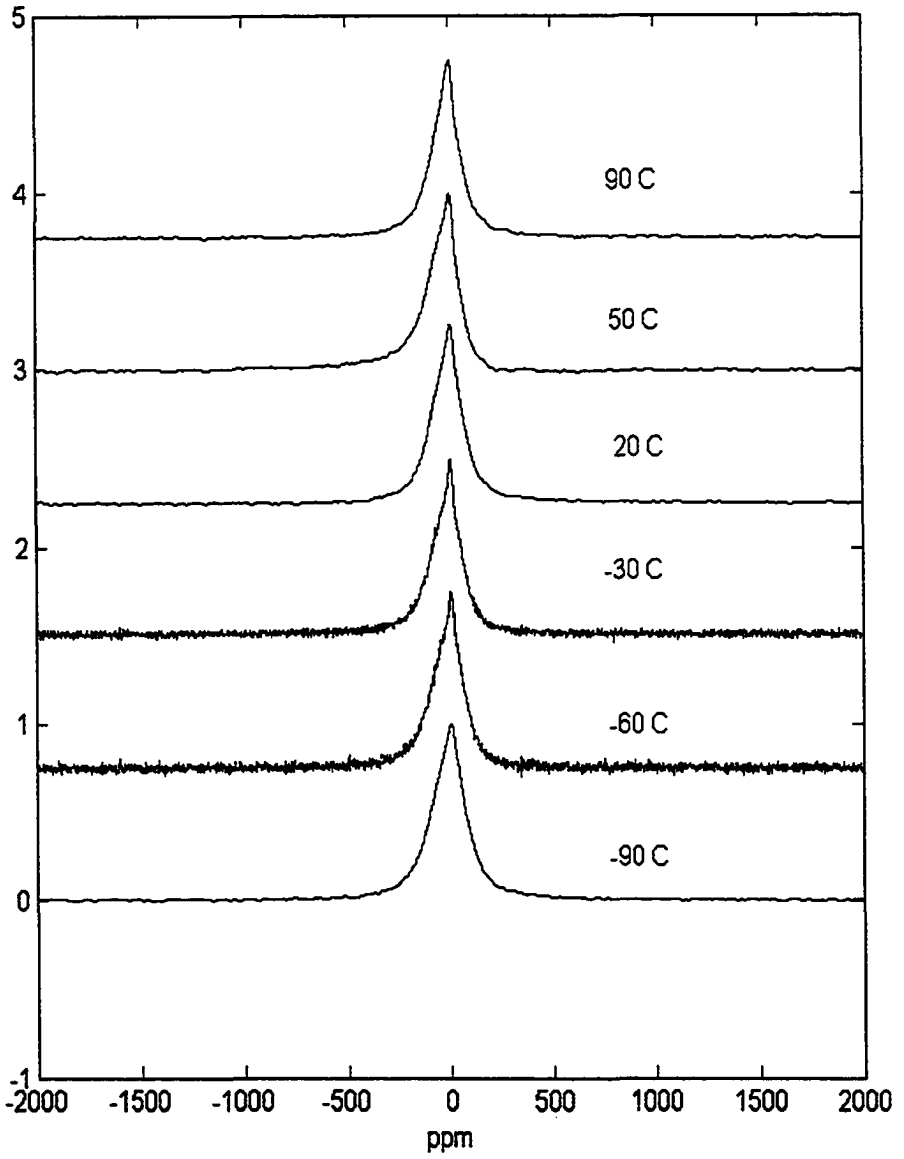

b: sample D

Fig. 4 Cont'd(sample C : EC:DMC = 70/30, sample D: EC / DMC = 30/70,)

In addition, as can be seen from Fig. 4, the chemical shifts do not change with temperature, but the line width decreases with increasing temperature. The quadrupole coupling constants (e^2qQ/h) and line width for ^7Li in sample C and D are presented in Table 2 as a function of temperature. As shown in Table 2, the quadrupole coupling constant decreases with increasing temperature, one of the possible explanation of this result is described as following.

Table 2.Temperature dependence of coupling constant, and line width

Sample C			Sample D		
Temperature (K)	Quadrupole Coupling constant (KHz)	Width (KHz)	Temperature (K)	Quadrupole Coupling constant (KHz)	Width (KHz)
183	35.53	11.39	183	39.4	18.83
213	31.48	13.52	213	38.58	18.74
243	31.47	13.05	243	37.82	18.27
323	28.88	11.39	323	37.30	18.00
363	26.65	10.14	363	31.98	17.14

(sample C : EC:DMC = 70/30, sample D: EC / DMC = 30/70,)

It is commonly believed that the temperature dependence of the quadrupole coupling constants C_q in graphite intercalation compound (GIC) might obey the equation [14]:

$$C_q(T) = C_q(0)[1 - \beta T^{3/2}], \beta > 0. \qquad (7)$$

Theoretical substantiation of this equation is related to temperature induced changes in root-mean-square displacements of atoms or in the phonon spectrum of the lattices [15]. Equation 7 implies that the quadrupole coupling constants C_q decreases with increasing temperature, consistent with the experimental results in Table 2.

4.4. Conclusions

^{7}Li NMR has been used to study the solid electrolyte interphase (SEI) on $LiNi_{0.8}Co_{0.2}O_2$ cathodes and mesocarbon microbead (MCMB) graphite anodes used in lithium ion cells over a wide temperature range. Changes in ^{7}Li NMR line width with decreasing temperature in sample A and B are very surprising. The nature of this unusual phenomenon is not yet well understood, and it seems to be linked to properties of the solid electrolyte interphase. Observed changes in SEI intensity with temperature are consistent with the EIS results, which would suggest that the nature of the electrolyte, electrolyte solvent content and the characteristic of SEI formed on electrodes, play a great role in determining the ability of lithium ion cells to withstand high temperature exposure without substantial irreversible capacity loss.

Chapter 5 The effect of electrolyte/solvent and electrode structure on the formation of the solid electrolyte interphase

The structure of electrode materials and electrolytes plays a key role in determining the performance of lithium ion batteries. The choice of electrolytes and electrolyte solvents is important not only in the conductivity but also, in the nature of the solid electrolyte interphase (SEI) resulting from electrolyte/solvent couple's interaction with electrode materials. In this chapter, we will further examine the effect of electrode structure, electrolyte and electrolyte solvent on formation of SEI on electrodes.

5.1. Introduction

As discussed in the previous chapter, the formation of SEI on electrodes strongly influences the performance of the battery, although the formation of a passive layer protects the electrodes from unwanted side reaction with electrolyte in the first few cycles. However, an uncontrolled passive SEI layer will lead to excessive loss of active lithium, which reduces specific capacity and can also increase the interfacial impedance to unacceptable levels. Therefore, studying relationships among the formation of SEI on electrodes, electrolyte, and electrode structure is important to improving battery performance.

The purpose of this study is to report ^{7}Li NMR and MAS NMR results on formation of SEI on different structure electrodes with different electrolytes

5.2. Experimental

GRD-AA-graphite (Timcal America Inc.) based anode, cathode made with lithium transition metal (TM) oxide compounds, with either 1 M $LiPF_6$ or 1 M lithium bis(oxalato)borate (LiBOB) electrolyte and solvent, were used to make lithium ion battery. The configuration of these batteries can be simply represented by:

GRD-AA-graphite (-)|electrolyte with different solvents|$LiTMO_2$ (+).

The samples studied were provided by Dr. Jun Liu of Argonne National Lab. The battery performance is summarized in Table 1. After this performance testing, the cells were disassembled in a helium glove box and electrodes were rinsed 3 times in DMC solvent.

For analysis, samples were packed in argon glove box. For the NMR measurements, anode and cathode electrode material were scraped off the copper current collector and aluminum screen, respectively. The details of NMR measurements have been described in Chapter 3.

5.3. Results and discussion

Fig. 1 shows wide line NMR spectra of the GRD-AA- graphite anode in different cell configuration but cell containing the same electrolyte and electrolyte solvent. It is

Table 1 Cell configuration and cell performance

Cell	Cathode	Anode	Electrolyte and solvent	Cell Performance
B1598	B1598c $Li_{1.06}Mn_{1.94}O_4$	B1598a graphite	1MLiBOB EC/DEC (1:1)	Charge to 4.2 V and discharge to 3.6V for 6cycles at 3 current level:8,12,16mA(2 cycles for each current level), cell cutoff at:3.4V
B1599	B1599c $LiNi_{.8}Co_{.15}Al_{.05}O_2$	B1599a graphite	1MLiBOB EC/DEC (1:1)	Charge to 4.1 V and discharge to 3.0V for 6 cycles at 3 current level:10,15, 20mA(2 cycles for each current level), cell cutoff at:3.0V
B1600	B1600c $LiNi_{1/3}Co_{1/3}Mn_{1/3}O_2$	B1600a graphite	1MLiBOB EC/DEC (1:1)	Charge to 4.3 V and discharge to 2.5V for 7 cycles at 4 current level:8 mA for one cycle15, 20 , 25 mA (2 cycles for each current level), cell cutoff at:2.5V
B1601	B1601c $LiNi_{1/3}Co_{1/3}Mn_{1/3}O_2$	B1601a graphite	1MLiPF$_6$ EC/MEC (3:7)	Charge to 4.3 V and discharge to 2.5V for 7 cycles at 4 current level:8 mA for one cycle15, 20 , 25 mA (2 cycles for each current level), cell cutoff at:2.5V

(EC ethylene carbonate, DEC: diethyl carbonate, MEC: methyl ethyl carbonate)

clearly seen from Fig. 1 that there is a very weak metallic band around 260 ppm and a main band around 0 ppm, accompanied by a small side bands. The 0 ppm band can be assigned to lithium nuclei, as in the lithium carbonate and lithium salts that are the main components of SEI, as shown by XPS and FTIR [1, 2]. In addition, a reversible intercalated lithium species, which would be characterized by Knight shifts of 40-50 ppm is not observed [3]. On the other hand, the similar location of the resonance band but different intensity indicates that the component of SEI is strongly dependent on electrolyte and electrolyte solvent.

Fig. 2 shows wide line spectra of GRD-AA- graphite anode in cells with different electrolyte and electrolyte solvents. These spectra are similar to those in Fig. 1. The ^{7}Li line width of the LiBOB-based cell are narrower than those of the $LiPF_6$ one. This is attributed to greater ionic or molecular motion in the SEI formed from the LiBOB-based electrolyte. In addition, the intensity of SEI in anode for the cell with $LiPF_6$ is greater than that for the cell with LiBOB-based electrolyte. This may suggest that the latter is more stable than the cell with $LiPF_6$.

High resolution MAS NMR spectra of anode in different cells are shown in Fig. 3. Fig. 3 exhibits the features of three bands for each sample. One band is located at around 0 ppm, discussed above in reference to the SEI. In addition, it should be pointed out that an SEI band having a chemical shift of 0 ppm indicates that surrounding ^{7}Li nuclei in the SEI have a finite value of electronic spin density and SEI has similar component and structure, because the NMR chemical shift of a radical is proportional to

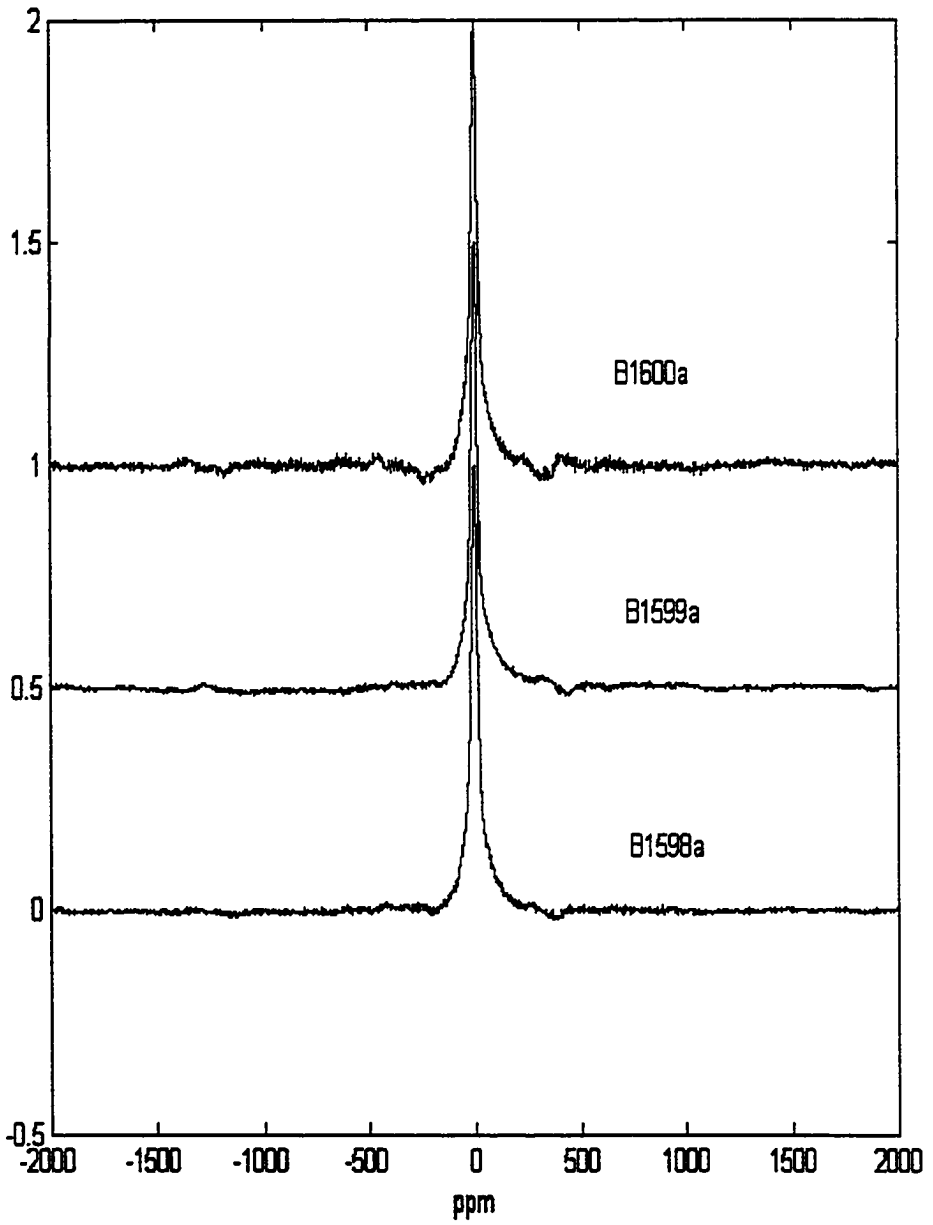

Fig. 1 ^{7}Li NMR wide line of sample B1598a, B1599a, B1600a, all these three samples containing 1MLiBOB EC/DEC (1:1).

the electric spin density at the position of the observed nuclei [4]. The band centered at around 50 ppm may be caused by the existence of multistage graphite intercalation compound (i.e., LiC_6 in stage 1, LiC_{12} in stage 2) [5, 6]. The band centered at around 260 ppm can be assigned to metallic lithium due to reduction of Li^+ to lithium [7]. This result show that the lithium has three different states during charge and discharge, that is, ionized lithium from SEI, intercalated lithium from intercalation compound, and metallic lithium from reduction.

Fig. 4 shows ^7Li NMR spectra of different cathodes in cells containing 1 M LiBOB electrolyte with EC/DEC electrolyte solvent. As one can see, all spectra display two peaks, one at around -26 ppm, which indicates SEI has similar properties on all three cathodes. However, the intensity of the SEI is in the order B1599c > B1600c > B1598c. This may indicate that it is easier to form the SEI on a layered structure sample (B1599c and B1600c). On the other hand, samples B1598c and B1600c contain Jahn-Teller Mn^{3+} ions, and the resulting Jahn-Teller distortion may inhibit the diffusion in the cathode which gives rise to SEI formation.

The peaks associated with lithium remaining in the active cathode material are located at 200, 170, and 160 ppm for sample B1598c and B1599c and B1600c, respectively. Evidently the chemical shift of B1598c is much greater than that of B1599c and B1600c. It is well known that the $Li_{1.06}Mn_{1.94}O_4$ (i.e., B1598c) compound shows a Jahn Teller distortion and charge ordering at room temperature. The chemical shift is proportional to spin density and $\frac{1}{r^3}$ (r is distance between nuclei). In addition, it

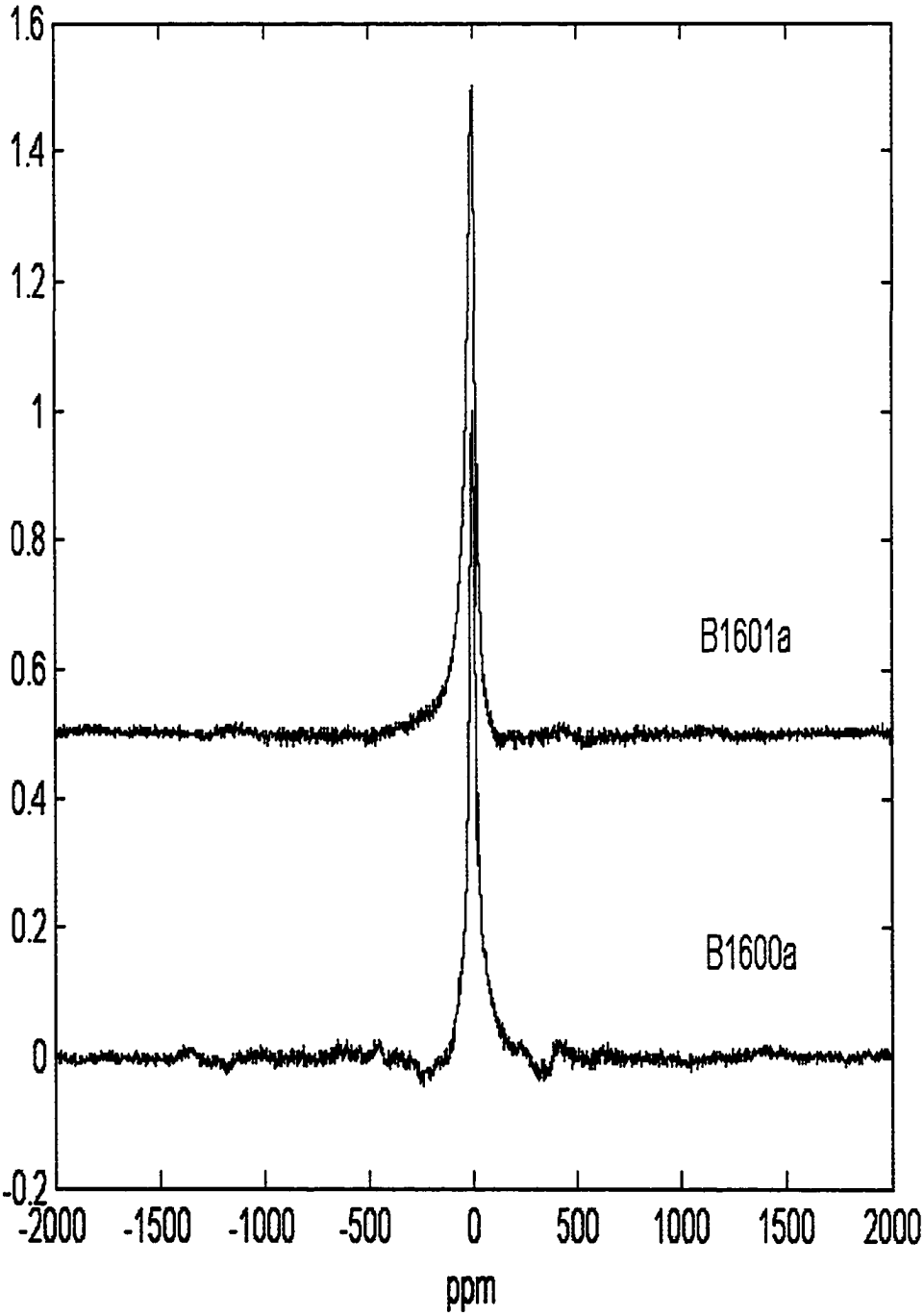

Fig. 2. ^{7}Li NMR for anode B1600a and B1601a in different electrolyte LiBOB (EC/DEC 1:1) and $LiPF_6$(EC/MEC:3:7), respectively.

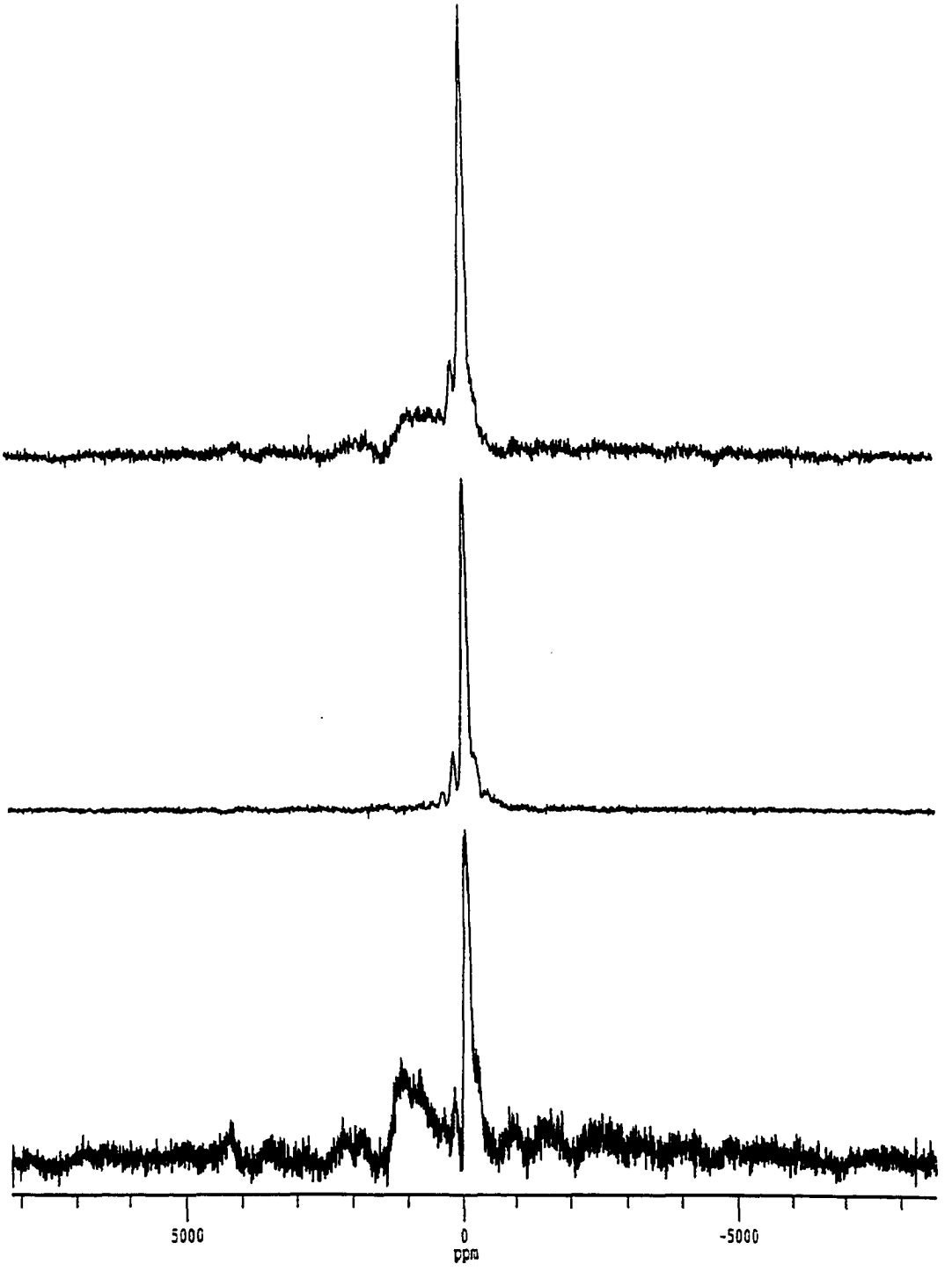

Fig. 3 ^{7}Li MAS NMR anode top B1601 bottom B1599 middle B1600a anode

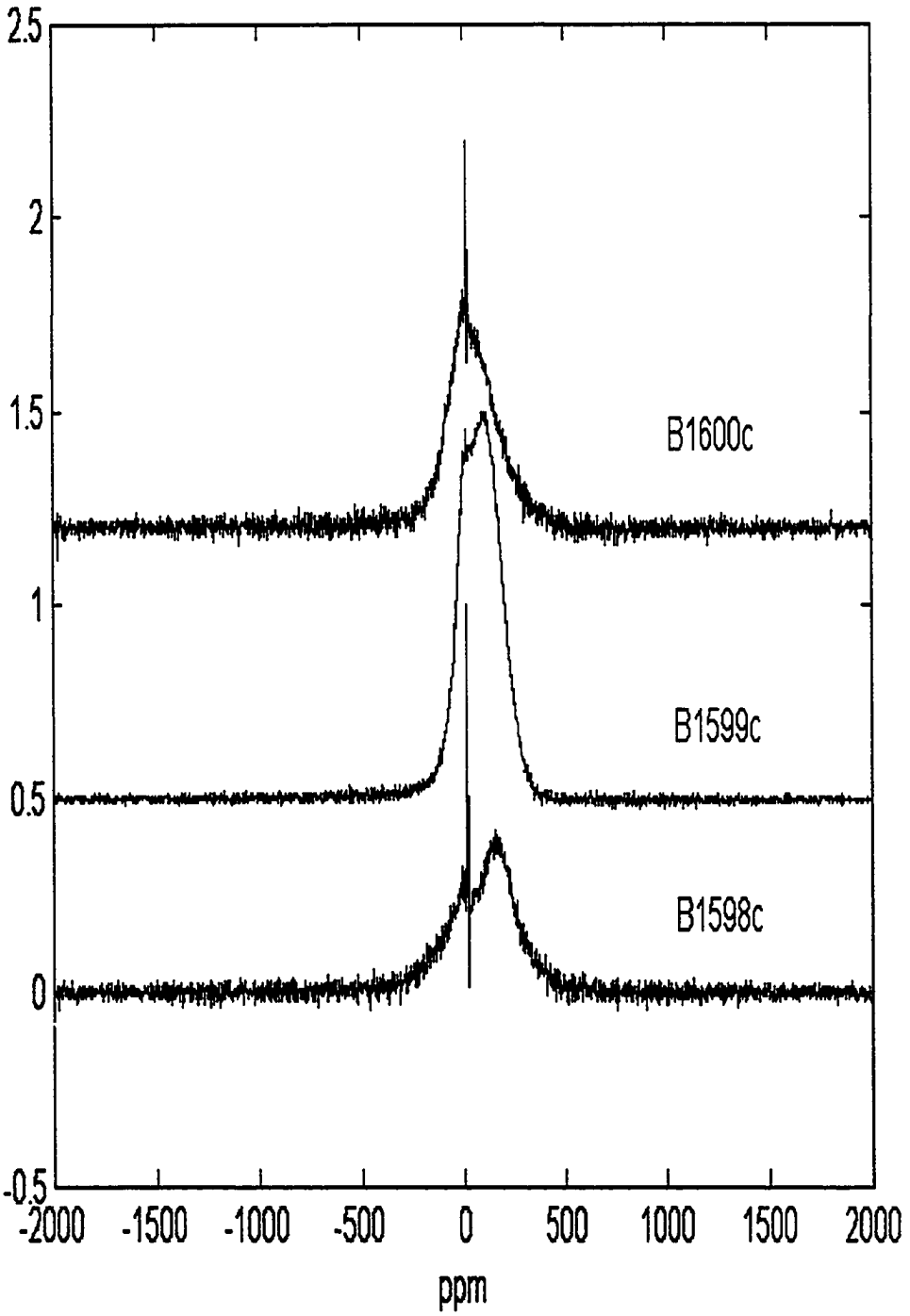

Fig. 4 ^{7}Li NMR spectra of B1598c, B1599c, and B1600c in 1M LiBOB EC/DEC (1:1)

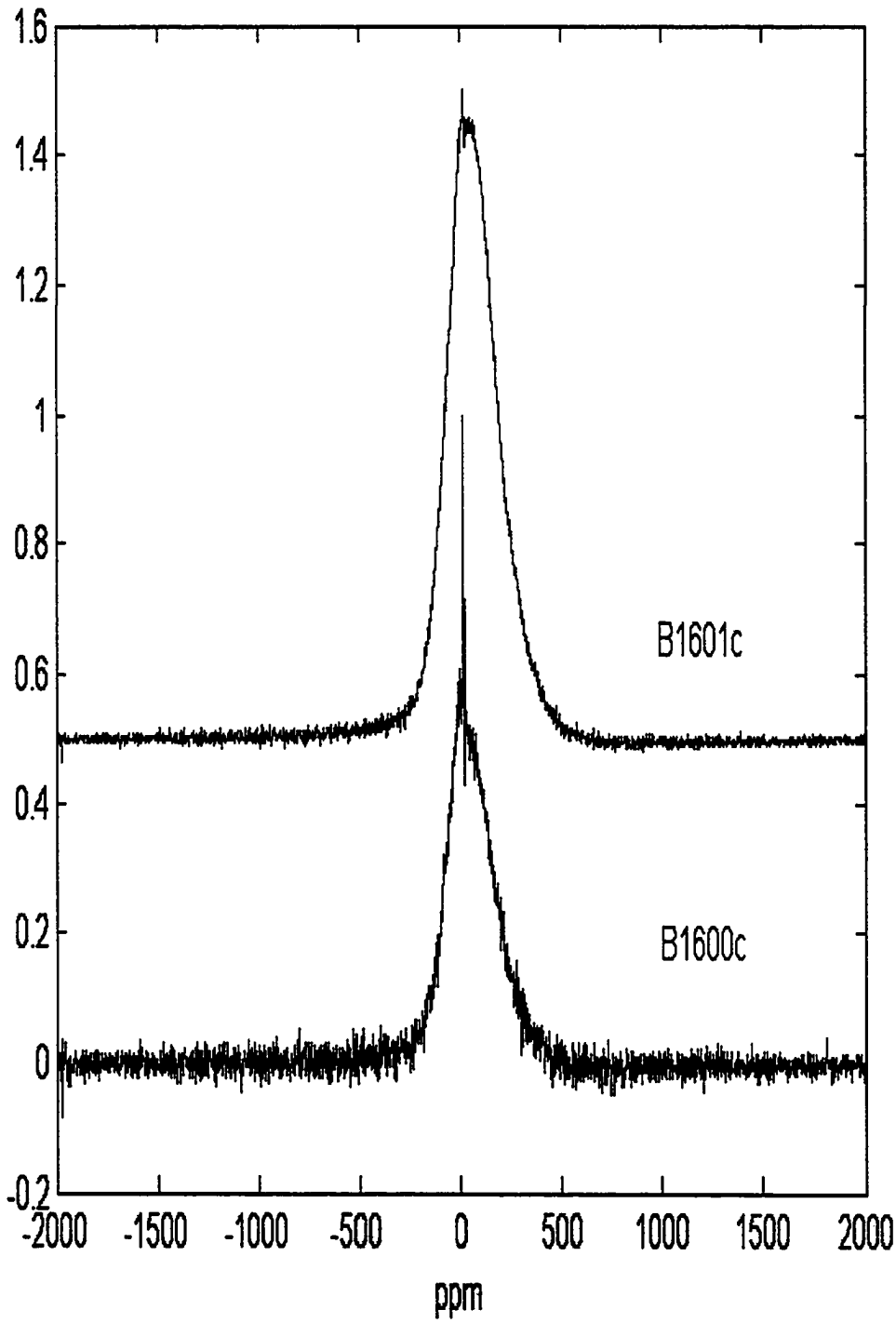

Fig. 5 ^{7}Li NMR spectra of B1600c and B1601c in different electrolyte ($LiPF_6$ and LiBOB)

should be pointed out that interaction of lithium into vacancies of the $Li_{1+x}Mn_2O_4$ causes a cooperative displacement of the lithium ions which are located at the 8a sites to neighboring vacant 16c sites and a simultaneous reduction of the host transition metal ions. This process results, in most cases, in an atacamite structure $(LiLi)_{16c}(MnMn)_{16d}O_4$ as described in references[8, 9]. On the other hand, as pointed out in the literature [10, 11], for lithium insertion into $Li_{1.06}Mn_{1.94}O_4$, a phase transformation from a cubic to a tetragonal symmetry occurs due to Jahn Teller distortion of a $Mn^{3+}O_6$ octahedron [12, 13].

^7Li NMR spectra of B1600c and B1601c (same cathode) in cells containing different electrolytes, namely 1M LiBOB and 1M $LiPF_6$, are shown in Fig. 5. Both spectra display a resonance at approximately the same chemical shift of -26 ppm due to SEI, but the SEI intensity is much larger in B1601c, with the 1M $LiPF_6$ electrolyte.

Fig. 6 shows ^7Li MAS NMR spectra of cathode B1600c, B1599c and B1598c. To study the local structure of lithium nuclei, we first describe the cation distributions in these three different cathodes. In layered notation, the cation distribution for these three

Compounds are $Li_{8a}[Mn_{1.94}Li_{0.06}]_{16d}O_4$, $Li_{(1-x)8a}[Co_{1/6}Ni_{1/6}Mn_{1/6}Lix]_{16d}$-$[Co_{1/6}Ni_{1/6}Mn_{1/6}]_{16d}O_4$, and $Li_{(1-x)8a}[Ni_{0.8}Co_{0.15}Al_{0.05}Li_x]O_2$, respectively. Peak 1, located at around -26 ppm unambiguously results from the SEI as discussed before. Peak 2 and 3 are usually assigned to lithium 8a sites and 16d sites or interstitial 16c sites, as confirmed by neutron diffraction [14]. Compared to ^7Li MAS NMR spectra of B1600c and B1599c, the ^7Li MAS NMR spectra of B1598c are further complicated due to the

Jahn-Teller effect. As one can expect, the chemical shift in lithium 8a sites in sample B1598c is greater than that of B1600c and B1599c. This means there are few paramagnetic ions such as low spin Ni^{3+} in nearest and second nearest of Li nuclei (8a sites). In other words, the surrounding Li nuclei (8a sites) have a few diamagnetic ions such as (Al^{3+}, Ni^{4+}, Co^{3+}) in the nearest and second nearest coordination. On the other hand, the complicated spectra of B1598c are also caused by insufficient spinning speed, because magic angle spinning at low speed cannot completely average the magnetic electron -nuclear interaction, as a result of which the broad peak is split into sideband manifolds.

The existence of mixed phase in different cathodes can be directly inferred from the coexistence of two line shapes indicated in Fig. 7. Though it is difficult to calculate the actual intensity in lithium of SEI and cathodes for different cells, these two line shapes suggest there are different Li environments in cells.

In conclusion, ^{7}Li NMR has been shown to be a useful tool to study SEI formation on electrodes in cells containing different electrolytes and solvents even though it can not directly SEI composition. That is, ^{7}Li NMR usually show a featureless line centered at 0 ppm for SEI on anodes and around -26 ppm on cathodes. However, NMR is quantitative, and it is relatively straightforward to determine the relative fraction of irreversible lithium in the SEI, compared to reversible lithium in electrodes.

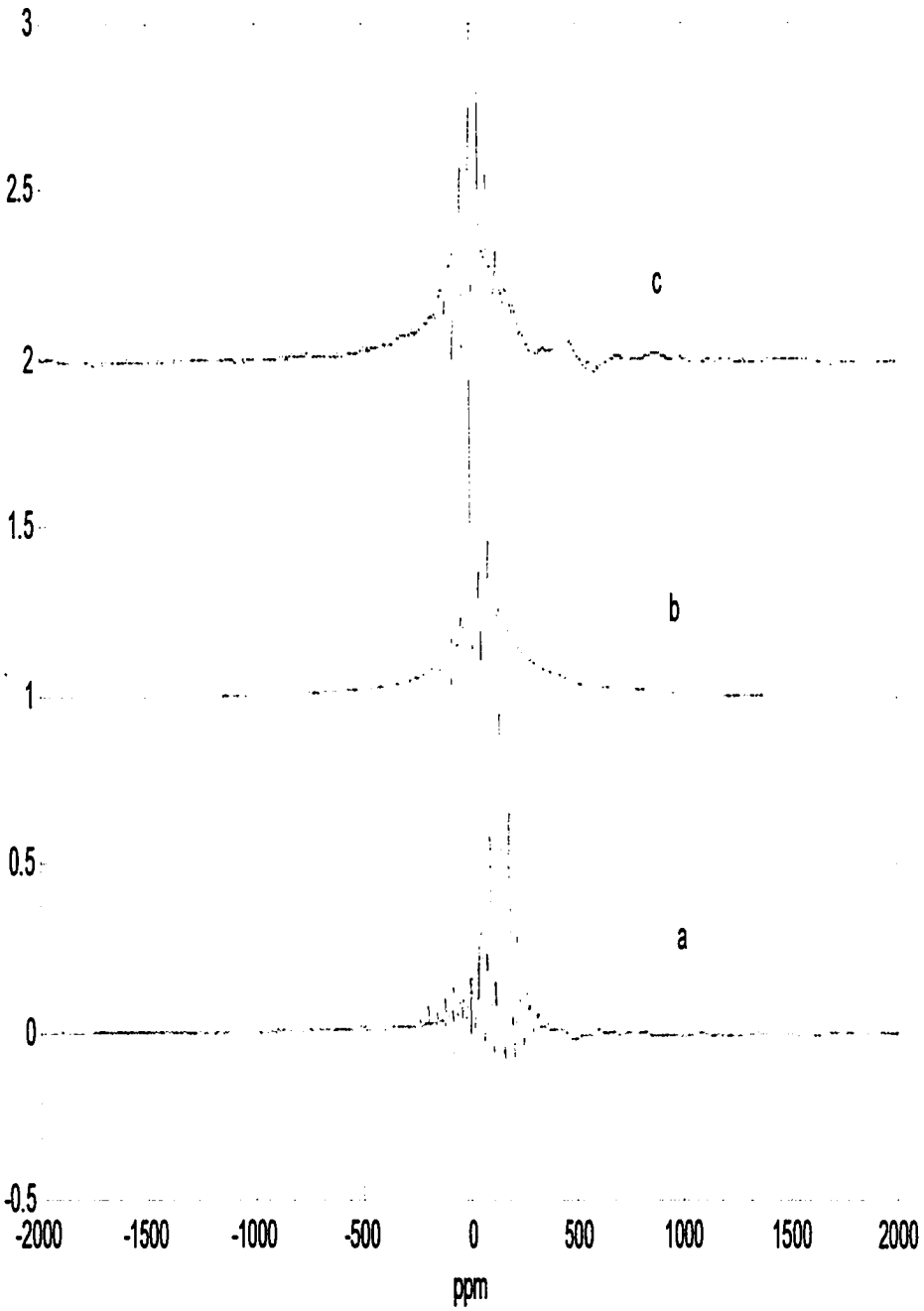

Fig. 6 ^{7}Li MAS NMR for cathode (a: B1598c , b:B1599c, c:B1601c)

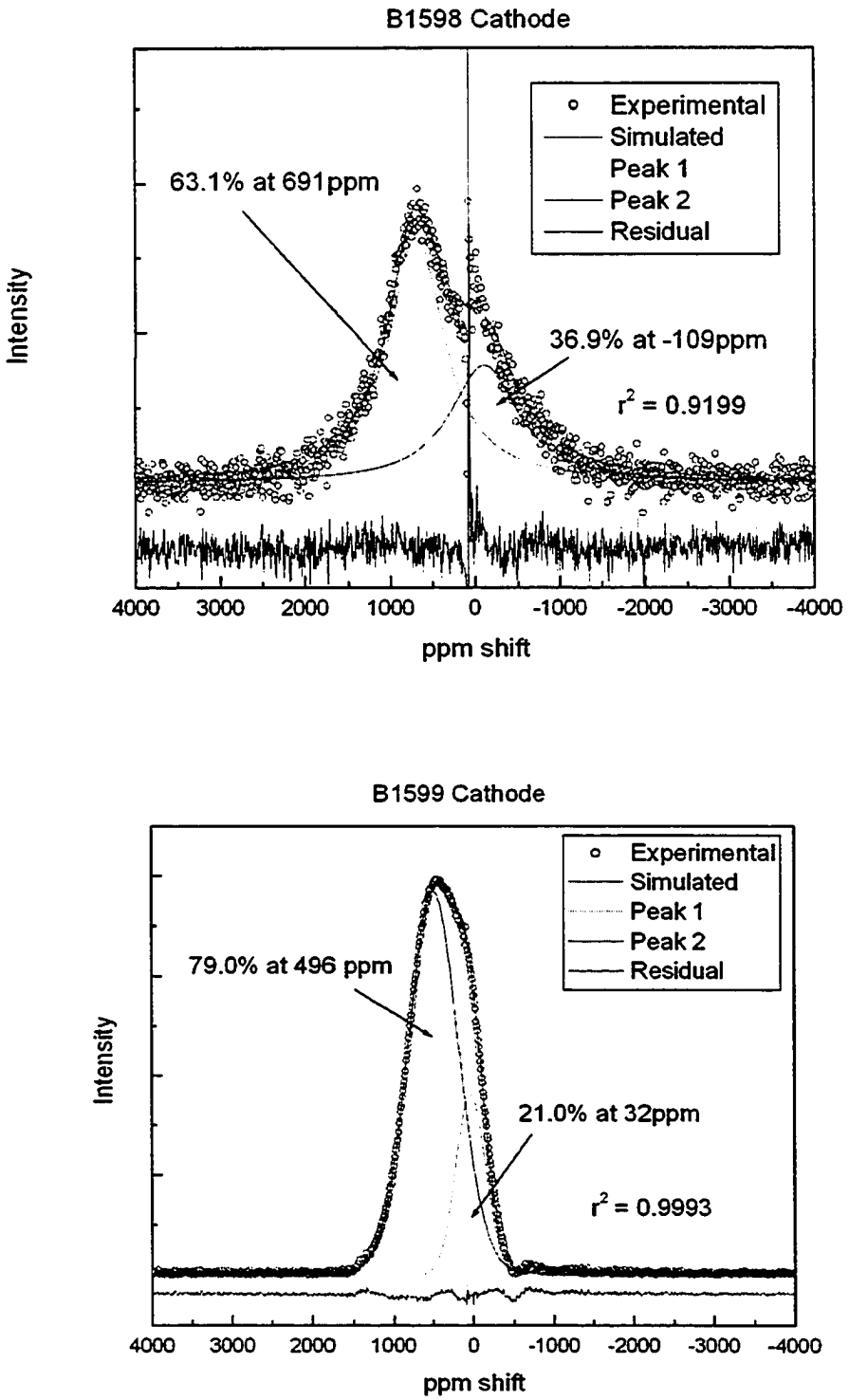

Fig. 7 Comparison of the experimental and best fit ^{7}Li NMR line shape for cathodes (B1598c, B1599c, B1600c, B1601c).

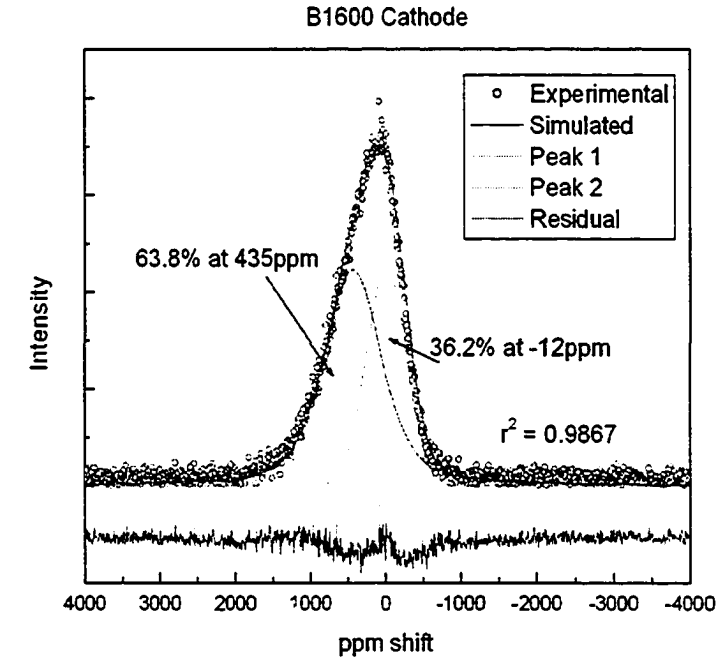

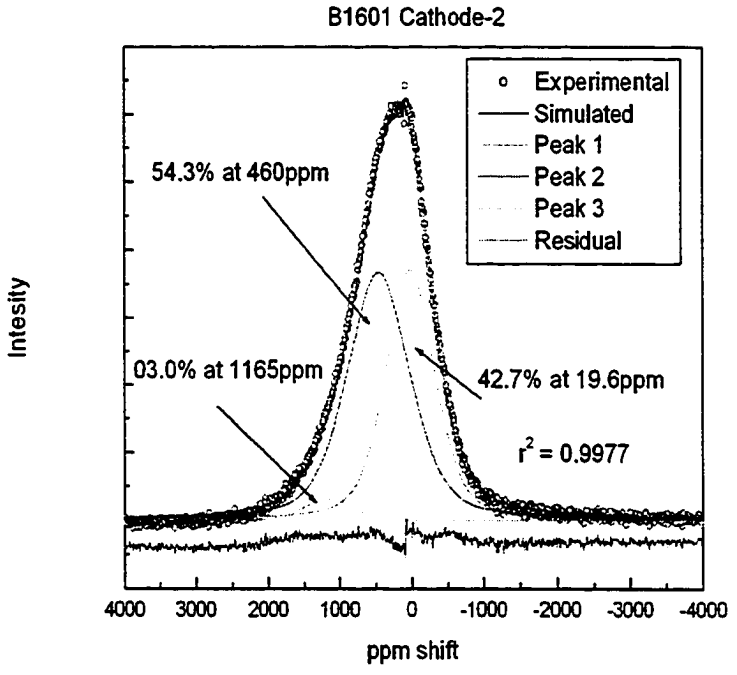

Fig. 7 Cont'd

Summary

In summary, this investigation provides direct EIS and NMR evidence that cell containing electrolyte with high EC content display less irreversible capacity after high temperature storage. The irreversible capacity is attributed to SEI growth on electrode surfaces. NMR results on cathodes, on the other hand, imply that the presence of Ni in cathode may reduce cell performance with electrode due to the oxidation of Ni^{3+} to Ni^{4+}. Our simulations show that a lower EC/DMC ratio is associated with a smaller SEI intensity for the cathode and higher intensity for the anode.

NMR measurements show that MCMB graphite based anodes exhibit high stability no chemical shift is evident over a wide temperature range. On cathodes, however, NMR does reveal changes in SEI intensity as a function of temperature. These changes are believed to be the result of decomposition of the SEI. Evidently, then, changes in the performance of the cell as a factor of temperature are, at least in part, due to changes in the SEI with temperature.

We report on the use of NMR to study the effect of electrolyte/solvent and electrode structure on SEI formation. The intensity of the SEI in a cell containing LiBOB electrolyte with EC and DEC is greater than that in a cell with $LiPF_6$ electrolyte with EC and DMC. This implies that the cell containing LiBOB electrolyte with EC and DEC is more stable. From the analysis of NMR of the cathode, it was found that it is easier to form SEI in layered structure cathode than in a spinel structure, suggesting that spinel structure materials may be better choices as cathode in lithium ion batteries. Evidently, then, the choice of electrolyte/solvent materials and electrode materials are key factors in determining the performance of lithium ion batteries.

References

Chapter 1

1. Curtis F.Holmes, Handbook of Solid State Batteries. (ed., M.Z.A. Munshi) World Scientific, 1995, p. 157.

2. Schlaikjer, C.R. and Liang, C.C. J. Electrochem. Soc., 118, 1447(1971)

3. Armand, M. Materials for Advanced Batteries, (ed., D. W. Murphy, J.Broadhead and B.C.H. Steele), Plenum Press, New York, 1980, p.145.

4. Lazzari, M. and Scrosati, B.J., J. Electrochem. Soc., 127, 773(1980)

5. A.J. Salkind, J.J. Kelley and A.G. Cannone, Handbook of Batteries, 2nd edn., (ed., D. Linden), McGraw Hill, New York, 1995, p. 241.

6. P.H.L. Notten and R.E.E. Einerhand, Adv., Mater., 3, 343 (1991)

7. L. Schwalbach and R. Riesterer, Appl. Phys. A, 32, 169(1983)

8. M.G.S.R.Tomass, W.I.F. David and J.B. Goodenough, Mater. Res. Bull., 20,1137 (1985)

9. B. Scrosati, Modern Batteries, 2nd edn., (ed., C.A.Vincent and B. Scrosati), London Arnold, 1997, p.275.

10. D.W.Murphy, Solid State Batteries, eds. C.A.C. Sequeira and A. Hooper, NATO ASI series (Martinus Nijhoff, 1985, p.181.

11. D.W.Murphy, Solid State Bionics, 18/19, 847 (1986).

12. Rachid Yazami and M.Z.A. Munshi, Handbook of Solid State Batteries. (ed., M.Z.A. Munshi), World Scientific, 1995, p.427.

13. J. Rouxel, J.Chim.Phys., 11/12, 86 (1983).

14. J.F. Fauvarque, "Chemical physics of intercalation" (ed.,A.P. Legrand and S.F. Landrois), NATO ASI series, Plenum Press, New York, 1987, p.291.

15. W. R. Mckinnon, Solid State Electrochemistry, ed. P.G. Bruce, Cambridge University Press, Cambridge, 1995, p.163.

16. J. Goodenough, Solid State Ionics, 69,184(1994).

17. T. Ohzuku and A. Ueda, J. Electrochem. Soc.,141, 2972 (1994).

18. G.G. Amatucci, J.M. Tarascon, D. Larcher and L.C. Klein, Solid State Iionics, 84, 169 (1996).

19. J. Livage, Chem., Mater., 3, 578 (1991).

20. Y.M. Li and T. Kudo, Solid State Ionics, 86/88, 1295 (1996).

21. K. Mizushima, P.C. Jones, P.J. Wiseman and J.B. Goodenough, Mater. Res. Bull., 15, 783 (1985)

22. J.N. Reimers and J.R. Dahn, J. Electrochem. Soc., 139, 2091 (1992).

23. R.E. Franklin, Acta Cryst., 4, 235(1951)

24. M. Balasubramanian, H.S. Lee, X. Sun, X.Q.Yang, A. Moodenbaugh, J. McBreen, D.A. Fisher, and Z. Fu, Electrochem. and Solid State Lett., 5 (1), A22 (2001)

25. B.V. Ratnakumar, M.C. Smart, S. Surampudi, J. Power Sources, 97/98,137(2001).

26. Yair Ein-Eli, Electrochem. and Solid State Lett., A206(2001)

27. A.M. Anderson, K. Edstrom, J.Electrochem. Soc., 148, A1100 (2001).

28. H.Z. Shoshan, Fuel and Energy Abstracts, 38, 161 (1997).

29. Y.Wang, V. Yufit, X. Guo, E.Peled, S Greenbaum, J. Power Sources, 94, 230 (2001)

30. A.V. Churikov, Electrochimica. Acta, 46, 2415 (2001)

31. A. Alliata, R. Kotz, P. Novak, H. Siegenthaler, Electrochem. Commun., 2, 436 (2000)

32. M. Inaba, Y. Kawatate, A. Funabiki, S-K. Jeong, T. Abe, Z. Ogumi, Electrochimica. Acta, 45, 99 (1999)

33. D. Zhao, et al, in preparation.

34. D. Zhao, X. Guo, M. Smart, S. Greenbaum, 202th ECS meeting, Oct, 2002, UT.

Chapter 2

1. K. Wulhrich, Encyclopedia of NMR, (ed., D.M.Grant and R.K.Harris), Wiley, London, 1996, Vol. 2, p.932.

2. E.M. Purcell, H.C. Torrey, and R.V. Pound, Phys.Rev., 69, 37 (1946).

3. F. Bloch, W.W. Hansen, M. Packard, Phys. Rev., 69, 127 (1946).

4. A. Abragam, The Principle of NMR, Oxford Univ. Press, 1961.

5. C.P. Slichter, The Principle of MR, Harper and row, New York, 1978.

6. C.P.Poole, Jr and H.A.Farach, The Theory of MR, John Wiley & Sons, New York, 1972.

7. J.H. Bartlett,Jr, J.J. Gibbons and R.E. Watson, Phys.Rev., 50, 315 (1936).

8. D.D. Laws, H.L. Bitter and A. Jerschow, Angew.Chem.Int.Ed., 41, 3096 (2002)

9. J.S. Rigden, Rev.Mod.Phys., 58(2), 433 (1986)

10. Z. Luz, P. Tekely and D.Reichert, Prog.in NMR Spectr., 41, 83 (2002)

11. R. Ditchfield, J. Chem. Phys. 56, 5688 (1972).

12. E. Fukushima and S.B.W. Roeder, Experimental Pulse NMR, Addison-Wesley, 1981.

13. T.C. Farrar, An Introduction to Pulse NMR Spectroscopy, Farragut Press, Chicago, 1987.

14. J. Keeler, Lecture Notes, University of Cambridge, 2002.

15. R.C. Jennison, Fourier Transforms and Convolutions, Pergamon Press, NY, 1961.

16. E.O. Brigham, The Fast Fourier Transform, Prentice-Hall, Englewood Cliffs, NJ, 1974.

17. A. Carrington and A.D. McLachlan, Introduction to Magnetic Resonance, Chapman and Hall, London, 1967.

Chapter 3

1. Y. Wang, X. Guo, S. Greenbaum, J. Liu, K. Amine, Electrochem. and Solid State Lett., 4(6), A69 (2001)

2. D. Zhao, et al, In preparation.

3. J.K.Owen, Chem. Soc. Rev., 26, 259 (1997)

Chapter 4

1. T. Ohzuku, A. Ueda, M. Kouguchi, J. Electrochem. Soc., 142, 4033 (1995)

2. J. M. Tarascon, M. Armand, Nature, 414(15), 359 (2001)

3. A. Alliata, R. Kotz, P. Novak, H. Siegenthaler, Electrochem. Commun., 2, 436(2000)

4. B. V. Ratnakumar, M. C. Smart, S. Surampudi, J. of Power Sources, 97/98, 137(2001)

5. M. Broussely, S. Herreyre, P. Kasztejna, K. Nechev, R. J. Staniewicz, J.Power Sources, 97/98, 13 (2001)

6. G. G. Amatucci, A. duPasquier, A. Blyr, T. Zheng, J. M. Tarascon, Electrochem. Acta, 45, 255 (1999)

7. M.C. Smart, B.V. Ratnakumar, S. Surampudi, H. Croft, D. Tice, and B. Staniewics, Ext. Abst. 201st ECS meeting, #455, San Francisco,CA, 2001.

8. D. Guyomard and J.M. Tarascon, J. Power Sources, 54, 92 (1995).

9.K. Zaghib, K. Tatsumi, Y. Sawada, S. Higuchi, H. Abe, T. Ohsak, J. Electrochem. Soc., 146, 2784(1999)

10. M.M. Thackeray, Prog. Solid State Chem., 25, 1 (1997).

11. C. Marichal, J. Hirschinger, P. Granger, M, Menetrier, A. Rongier, C. Delmas

Inorg. Chem., 34, 1773 (1995)

12. D. Zhao, et al, in preparation.

13. N. Bloembergen, E. M. Purcell, R. V. Pound, Phys. Rev. 73, 679(1948)

14. T. P. Das and P.C. Schmidt, Z. Naturforsch. 42a, 47 (1986)

15. V. P. Tarasov, Yu. B. Muravlev and K.E. Guerman, J. Phys., : Condens. Matter,13, 1041(2001).

Chapter 5

1. A.M. Andersson, and K. Edstrom, J.Electrochem.Soc. 148(10), A1100 (2001).

2. S. Genies, R. Yazami, and J. Garden, Synth.Metals, 93, 77(1998).

3. K. Zaghib, K. Tatsumi, Y. Sawada, S. Higuchi, H .Abe, and T. Ohsak, J. Electrochem. Soc, 146, 2784 (1999).

4. C.J. Pickard, Phys. Rev., 63, 245101 (2001).

5. J. Conard, V.A. Nalimova, D. Guerard, in "extended abstract of the 7th Intern. Symposium on intercalation compound" (Ed., J.P.Issi,) Louvain-La, Neuve. 1993, p.114.

6. M. Galia, J. Phys. Chem. B,105(13), 2534 (2001).

7. J. Conard and H. Estrade, Mater.Sci.Eng., 31, 173 (1997).

8. D.W. Murphy, R.J. Cava, S.M. Zahurak and A. Santoro, Solid State Ionic, 9/10, 413 (1983)

9. G. Pistoia, M. Pasquali, L.A. dePicciotto and M.M. Thackeray, Solid State Ionic, 28, 879 (1988)

10. T. Ohzuku, M. Kitagawa and T .Hirai, J.Electrochem.Soc., 137, 769 (1990)

11. M.M. Thackeray, W.I.F .David, P.G. Bruce and J.B. Goodenough, Mater. Res. Bull., 18, 461(1983)

12. B.E. Douglas and C.A. Hollingworth, Symmetry in Bonding and Spectra, Academic Press, (1985), p.226.

13. P.A. Cox, The Electronic Structure and Chemistry o f Solids, ch.5, Oxford University Press, 1987.

14. H. Berg, E.M. Kelder, and J.O. Thomas, J.Mater.Chem.9, 427 (1999)